A&A 626, A92 (2019)
https://doi.org/10.1051/0004-6361/201833920

Astronomy & Astrophysics

30-micron sources in galaxies with different metallicities*

M. Gładkowski[1], R. Szczerba[1], G. C. Sloan[2], E. Lagadec[3], and K. Volk[4]

[1] Nicolaus Copernicus Astronomical Center, ul. Rabiańska 8, 87-100 Toruń, Poland
e-mail: seyfert@ncac.torun.pl
[2] Astronomy Department, Cornell University, Ithaca, NY 14853-6801, USA
[3] Laboratoire Lagrange, UMR7293, Université Côte d'Azur, CNRS, Observatoire de la Côte d'Azur, Boulevard de l'Observatoire, 06304 Nice Cedex 4, France
[4] Space Telescope Science Institute, 3700 San Martin Drive, Baltimore, Maryland, USA

Received 20 July 2018 / Accepted 14 December 2018

ABSTRACT

Aims. We present an analysis and comparison of the 30 μm dust features seen in the *Spitzer* Space Telescope spectra of 207 carbon-rich asymptotic giant branch (AGB) stars, post-AGB objects, and planetary nebulae (PNe) located in the Milky Way, the Magellanic Clouds (MCs), or the Sagittarius dwarf spheroidal galaxy (Sgr dSph), which are characterised by different average metallicities. We investigated whether the formation of the 30 μm feature carrier may be a function of the metallicity. Through this study we expect to better understand the late stages of stellar evolution of carbon-rich stars in these galaxies.
Methods. Our analysis uses the "Manchester method" as a basis for estimating the temperature of dust for the carbon-rich AGB stars and the PNe in our sample. For post-AGB objects we changed the wavelength ranges used for temperature estimation, because of the presence of the 21 μm feature on the short wavelength edge of the 30 μm feature. We used a black-body function with a single temperature deduced from the Manchester method or its modification to approximate the continuum under the 30 μm feature.
Results. We find that the strength of the 30 μm feature increases until dust temperature drops below 400 K. Below this temperature, the large loss of mass and probably the self-absorption effect reduces the strength of the feature. During the post-AGB phase, when the intense mass-loss has terminated, the optical depth of the circumstellar envelope is smaller, and the 30 μm feature becomes visible again, showing variety of values for post-AGB objects and PNe, and being comparable with the strengths of AGB stars. In addition, the AGB stars and post-AGB objects show similar values of central wavelengths – usually between 28.5 and 29.5 μm. However, in case of PNe the shift of the central wavelength towards longer wavelengths is visible. The normalised median profiles for AGB stars look uniformly for various ranges of dust temperature, and different galaxies. We analysed the profiles of post-AGB objects and PNe only within one dust temperature range (below 200 K), and they were also similar in different galaxies. In the spectra of 17 PNe and five post-AGB objects we found the broad 16–24 μm feature. Two objects among the PNe group are the new detections: SMP LMC 51, and SMP LMC 79, whereas in the case of post-AGBs the new detections are: IRAS 05370-7019, IRAS 05537-7015, and IRAS 21546+4721. In addition, in the spectra of nine PNe we found the new detections of 16–18 μm feature. We also find that the Galactic post-AGB object IRAS 11339-6004 has a 21 μm emission. Finally, we have produced online catalogues of photometric data and *Spitzer* IRS spectra for all objects that show the 30 μm feature. These resources are available online for use by the community.
Conclusions. The most important conclusion of our work is the fact that the formation of the 30 μm feature is affected by metallicity. Specifically that, as opposed to more metal-poor samples of AGB stars in the MCs, the feature is seen at lower mass-loss rates, higher temperatures, and has seen to be more prominent in Galactic carbon stars. The averaged feature (profile) in the AGB, post-AGB objects, and PNe seems unaffected by metallicity at least between a fifth and solar metallicity, but in the case of PNe it is shifted to significantly longer wavelengths.

Key words. catalogs – stars: AGB and post-AGB – planetary nebulae: general – galaxies: individual: Milky Way – Magellanic Clouds – galaxies: individual: Sagittarius Dwarf Spheroid galaxy

1. Introduction

Low and intermediate-mass stars (from ~0.8 to ~8 $M_\odot$) terminate their evolution on the asymptotic giant branch (AGB) in a phase of intense mass-loss. During this evolutionary phase, the star is obscured by a thick envelope made of gas and dust, and is mainly or even only visible in the infrared.

AGB stars produce carbon in their helium-burning shells, which is brought to the surface by a series of dredge-ups (see e.g. Herwig 2005). The chemical composition of the outer layers of the star depends mostly on their C to O abundance ratio. When the C/O value exceeds unity, the star becomes carbon-rich. Most of the available oxygen is locked in the very stable CO molecule, and the leftover carbon forms molecules typical for carbon stars such as C_2, C_2H_2, and HCN, as well as carbon-rich dust grains. Groenewegen et al. (1995) demonstrated that Galactic stars with initial masses $M_* \lesssim 1.55\ M_\odot$ never become carbon stars. However, the formation of carbon-rich stars also depends on the metallicity of the host galaxy (see e.g. Fig. 3 in Piovan et al. 2003). At lower metallicity, stars with initial masses down to 1.1 $M_\odot$ could become carbon-rich. For example, $Z = 0.004$, as for the Sagittarius dwarf spheroidal galaxy (Sgr dSph) or the Small Magellanic Cloud (SMC).

During the post-AGB phase, when the high mass-loss phase has terminated, the ejected envelope moves away from the star,

* Tables D.1–D.6 are only available at the CDS via anonymous ftp to cdsarc.u-strasbg.fr (130.79.128.5) or via http://cdsarc.u-strasbg.fr/viz-bin/qcat?J/A+A/626/A92

which can become visible in the optical. When the mass of the H-rich envelope decreases to about 0.001 of solar mass for 0.6 $M_{\odot}$, the star moves quickly to the left on the H–R diagram (increases its temperature) at nearly constant luminosity (see e.g. Frankowski 2003). Afterwards, the star can ionise the surrounding matter and a planetary nebula (PN) is formed. The mass-loss process in low- and intermediate-mass stars is one of the most important mechanisms to provide enriched gas and dust to the interstellar medium for a new generations of stars.

A broad-emission dust feature peaking at around 30 μm is only seen in the spectra of some carbon-rich AGB stars, post-AGB stars, and PNe. This feature was observed for the first time by Forrest et al. (1981), who discovered it in CW Leo, IC 418 and NGC 6572. Since its discovery, it has been detected in many carbon-rich objects. In carbon-rich post-AGB objects, this feature can sometimes be observed along with the still-unidentified 21 μm feature.

Goebel & Moseley (1985) proposed solid magnesium sulphide (MgS) as the possible carrier of the 30 μm emission feature. Despite the MgS identification being generally accepted by the community (e.g. Hony et al. 2002; Zijlstra et al. 2006; Lombaert et al. 2012; Sloan et al. 2014, 2016), its identification remains a matter of some debate. For instance, Zhang et al. (2009) have argued that the abundance of MgS is not sufficient to explain the strength of the feature in the post-AGB star HD 56126. The amount of MgS mass required to explain the power emitted by the 30 μm feature in this object would require ten times more atomic sulphur than available in the ejected envelope. On the basis of a sample of extreme carbon stars, Messenger et al. (2013) found a correlation between the 30 μm feature and the 11.3 μm silicon carbide (SiC) one, which suggests that the abundance of the carrier of the 30 μm feature is linked to the SiC abundance. On the basis of fullerene-containing planetary nebulae, Otsuka et al. (2014) suggested that graphite can also be the carrier of this feature, because it exhibits a very broad, strong feature peaking around 30–40 μm (see also Speck et al. 2009). Other materials have also been proposed as carriers of the 30 μm feature. Grishko et al. (2001) proposed hydrogenated amorphous carbon (HAC) as a possible carrier. Duley (2000) suggested that the 30 μm feature may be indicative of carbon-based linear molecules with specific side groups. However, the hypothesis that MgS is responsible for the 30 μm feature is not ruled out. This is partly because the optical properties of MgS in the optical and ultraviolet range are still unknown, preventing modellers from properly estimating temperature inside the envelope. In addition, the shape of MgS grains is important. For example, Hony et al. (2002) concluded that the shape of the 30 μm feature can be best reproduced when the MgS grains are not perfect spheres. In addition, Lombaert et al. (2012) suggested that MgS condenses as a coating on the top of amorphous carbon and SiC grains. Using their model it is possible to resolve the MgS mass problem. However, Szczerba et al. (1997), showed that for the simple spherical coating the feature has two peaks, which seems not to be observed (see their Fig. 3).

Hony et al. (2002) have analysed in a uniform way a sample of 63 Galactic 30 μm sources observed by the Infrared Space Observatory (ISO). Before Sloan et al. (2016) this was the largest sample analysed in a uniform way. The *Spitzer* Space Telescope mission (hereafter *Spitzer*), thanks to its sensitivity, was able to detect distant sources with 30 μm features in our Galaxy (designated on all the figures in this paper by the short name "GAL"), but also in nearby galaxies such as the SMC, Large Magellanic Cloud (LMC), and the Sgr dSph. On the basis of the *Spitzer* spectra, Sloan et al. (2016) have analysed a sample of 184 carbon stars in the Magellanic Clouds (MCs), and about 50% of them show the 30 μm emission.

In this paper we present a uniform analysis of the 30 μm feature, on the basis of the spectra from the InfraRed Spectrograph (IRS) on board *Spitzer* for carbon-rich sources from the Milky Way and the three nearby galaxies mentioned above. All of these galaxies are characterised by the different average metallicities. Therefore we can compare the basic properties of this feature in various environments.

Our paper is organised as follows. In Sect. 2, we describe the sample and our catalogues of 30 μm sources. In Sect. 3 we describe the method for fitting the continuum to the spectra. We then explain how we determine the properties of the 30 μm feature and present a description of the contents of the tables with the results. In Sect. 4 we show the correlation study between the properties of the 30 μm feature for the different populations of the objects. The second part of this section contains the summary of the results we have obtained.

2. Spectral sample

2.1. Target selection and the full sample

Our sample consists of archival data obtained by the InfraRed Spectrograph (IRS), on board *Spitzer*. The sample considered in this paper is quite similar to the sample of 30 μm sources described by Sloan et al. (2014, 2016) as far as the SMC and LMC objects are concerned. In case of Sgr dSph and Milky Way objects the samples were selected from different authors. Details of our selection are given in Appendix A.

Our full sample consist of 207 objects in total: five from the Sgr dSph (four AGB stars, one PN), 22 from the SMC (eight AGB stars, three post-AGB objects, and 11 PNe), 121 from the LMC (83 AGB stars, 17 post-AGB objects, and 21 PNe), and 59 objects from our Galaxy (17 AGB stars, 23 post-AGB objects, and 19 PNe).

The majority of our objects were observed in the low resolution (R ~ 60–120) mode during various observational programs. These spectra have two short-low (SL) and two long-low (LL) modules, which provide spectral coverage from ~5–38 μm, and join together around 14 μm. The SL and LL modules each have their own two apertures, one for the second order spectrum (5.2–7.7 μm and 14–21.3 μm) and one for the first order spectrum (7.4–14.5 μm and 19.5–38 μm; see Lebouteiller et al. 2011 for more details). The telescope had to shift position to put the target in each of the four apertures, which requires eight pointings. Some of the objects were observed in the high resolution modules (see e.g. Lebouteiller et al. 2015), short-high (SH) and long-high (LH), which cover the spectral ranges from ~10–37 μm (9.9–19.6 μm and 18.7–37.2 μm, respectively) at the resolution of ~300.

For both resolutions a jump between the short segments (SL/SH) and long segments (LL/LH) of the spectra is common. This jump is observed in partially extended sources when reduced using the point-like source flux calibration. For such objects, the LL/LH spectrum contains more flux than the SL/SH, because the LL/LH extraction aperture is larger than the SL/SH (this problem is described by Lebouteiller et al. 2011 in the case of low resolution spectra). Discontinuities were removed between orders by multiplying each spectral segment by a scaling factor to align them in the regions of overlap. In almost all cases the corrections are made up to the brightest segment, on the grounds that it is the one best centred in the slit.

Table 1. Sgr dSph sample.

Name	Other name	(J2000.0) RA (deg)	Dec (deg)	Position reference	Class	Period (days)	Period reference	Program ID	AOR key
Sgr 3	IRAS F18413-3040	281.129	−30.619	2MASS	C-AGB	446	(1)	30333	18054656
Sgr 7	IRAS F18436-2849	281.715	−28.764	2MASS	C-AGB	512	(1)	30333	18054912
Sgr 15	IRAS F18555-3001	284.683	−29.949	2MASS	C-AGB	417	(1)	30333	18055168
Sgr 18	IRAS 19013-3117	286.148	−31.216	2MASS	C-AGB	485	(1)	30333	18055424
Wray16-423	PN G006.8-19.8	290.544	−31.511	2MASS	C-PN, 16–24 μm feat. [(a)]	...	...	50261	25833216

Notes. The table lists: names, coordinates, reference position, classification of spectra (C-AGB: carbon-rich AGB star, C-pAGB: carbon-rich post-AGB star, C-PN: carbon-rich planetary nebula), period with reference, program identifier, and AOR key. The tables with the Galactic and MCs objects are available in Appendix D. [(a)] Otsuka (2015).
References. (1) Lagadec et al. (2009).

The data reduction for the spectra in the MCs followed the standard Cornell algorithm described in detail by Sloan et al. (2012). The key element is the optimal extraction of the spectra from the background-subtracted and cleaned spectral images (Lebouteiller et al. 2010). The spectra of sources in the Galaxy and the Sgr dSph were obtained from the Combined Atlas of Sources with *Spitzer* IRS Spectra (CASSIS[1]; Lebouteiller et al. 2011, 2015), which used a similar approach, including optimal extraction.

Table 1 lists basic information about objects in the Sgr dSph. Appendix D presents the Tables D.1–D.3 with basic information about objects from the SMC, LMC, and Milky Way. The objects which are marked by the bold face names in Tables 1, and D.1–D.3, are excluded from further analysis for reasons described in Sect. 3.1.

In each of these tables we present the name of the object, another common name if available, RA and Dec coordinates in the J2000 system, its position reference, classification of the object (Class), and its main period if known with the corresponding references. The position reference is IRAC for SMC and LMC sources and 2MASS[2] for Galactic and Sgr dSph objects (see Sect. 2.2 for details). The column with the classification contains any additional information about the sources and the references (if needed). For the post-AGB objects we put the name of the group for the object (see Sect. 3.1 for details), then we mark objects with 21 μm feature, C_2H_2 band, and objects showing the broad 16–24 μm feature. In a case of PNe we put information about presence of the 16–18 μm feature, broad 16–24 μm feature and the fullerenes. In the Galactic sample we indicate the S-type stars. Finally, Program ID and AOR keys (*Spitzer* Astronomical Observation Request) for each source are given.

2.2. Toruń catalogues of 30 μm objects

We have produced online catalogues of photometric data and *Spitzer* IRS spectra for all objects that show the 30 μm feature. The 207 objects are organised into three different catalogues: 22 objects from the SMC, 121 from the LMC, and 59 Galactic sources. The five Sgr dSph objects are listed along with the Galactic catalogue and they are distinguished there by the special comments. Each part of our database is available online at:

– http://www.ncac.torun.pl/30smc
– http://www.ncac.torun.pl/30lmc
– http://www.ncac.torun.pl/30galactic

The structure of the catalogues is similar to the evolutionary catalogue of Galactic post-AGB and related objects, created by Szczerba et al. (2007, 2012). After entering any of the catalogue links given above, the home screen will appear. The user has to click on the main button "30 micron SMC/LMC/Galactic" depending on the version. After this action, a new screen appears with the information about the total number of objects in this section of the catalogue and list of objects ordered according to increasing right ascension (Col. 1). In addition, the other names, if any (Col. 2), classification (Col. 3), explanations to each object (e.g. information about variability) and the bibliography (Cols. 4 and 5, respectively) are given. The bibliography contains the link to SAO/NASA Astrophysical Data System (ADS). After clicking it, the list of papers for a given object appears.

The main bar above the list of objects contains the following buttons (starting from the left):
– Home – allows the user to get back to the home screen;
– Change catalogue – allows the user to change the sub-catalogue to a different one;
– Info – show more information about the catalogue content;
– Search – allows the user to search the sub-catalogue using different criteria (name, class, coordinates, etc.);
– Export – allows the user to export the data (see below for details).

After clicking on the RA/Dec value of a given object, a new screen appears with all the characteristics. The main bar on the top of the screen remains unchanged. These characteristics are divided into three categories: "Astrometric data" with the names and coordinates in degrees obtained for a few photometric surveys; "Photometric data" with a photometry provided by these surveys; and "Spectroscopic data" containing the information about available spectra for a given object. An example of the screen showing all the information for a given object is shown in Fig. 1. Inside the panel with the photometric data, there are two "SED" buttons, which allows the user to see the spectral energy distribution (SED) in (Jy) or in (erg cm^{-2} s^{-1}), as a function of wavelength (μm). The photometry is represented by the points on this diagram, whereas the *Spitzer* spectrum is overplotted as the solid line in the corresponding units. The data in our catalogue can be exported by clicking on the "Export" button (see Fig. 1). The possible format of the exported table is ascii or Excel.

[1] CASSIS database is available online at: http://cassis.sirtf.com/atlas/welcome.shtml
[2] 2MASS: The Two Micron All Sky Survey.

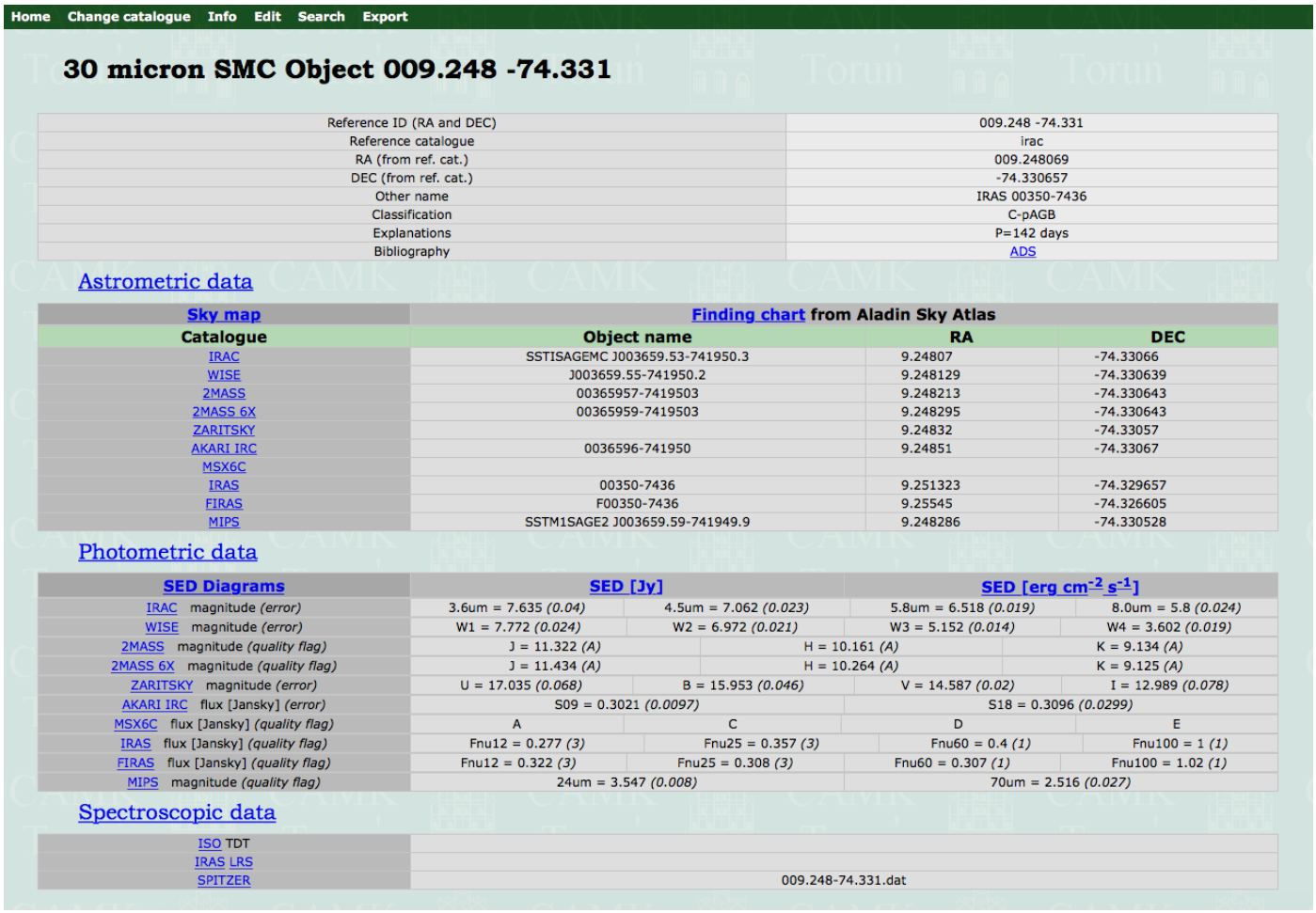

Home Change catalogue Info Edit Search Export

30 micron SMC Object 009.248 -74.331

Reference ID (RA and DEC)	009.248 -74.331
Reference catalogue	irac
RA (from ref. cat.)	009.248069
DEC (from ref. cat.)	-74.330657
Other name	IRAS 00350-7436
Classification	C-pAGB
Explanations	P=142 days
Bibliography	ADS

Astrometric data

Sky map	Finding chart from Aladin Sky Atlas		
Catalogue	**Object name**	**RA**	**DEC**
IRAC	SSTISAGEMC J003659.53-741950.3	9.24807	-74.33066
WISE	J003659.55-741950.2	9.248129	-74.330639
2MASS	00365957-7419503	9.248213	-74.330643
2MASS 6X	00365959-7419503	9.248295	-74.330643
ZARITSKY		9.24832	-74.33057
AKARI IRC	0036596-741950	9.24851	-74.33067
MSX6C			
IRAS	00350-7436	9.251323	-74.329657
FIRAS	F00350-7436	9.25545	-74.326605
MIPS	SSTM1SAGE2 J003659.59-741949.9	9.248286	-74.330528

Photometric data

SED Diagrams	SED [Jy]		SED [erg cm^{-2} s^{-1}]	
IRAC magnitude *(error)*	3.6um = 7.635 *(0.04)*	4.5um = 7.062 *(0.023)*	5.8um = 6.518 *(0.019)*	8.0um = 5.8 *(0.024)*
WISE magnitude *(error)*	W1 = 7.772 *(0.024)*	W2 = 6.972 *(0.021)*	W3 = 5.152 *(0.014)*	W4 = 3.602 *(0.019)*
2MASS magnitude *(quality flag)*	J = 11.322 *(A)*	H = 10.161 *(A)*	K = 9.134 *(A)*	
2MASS 6X magnitude *(quality flag)*	J = 11.434 *(A)*	H = 10.264 *(A)*	K = 9.125 *(A)*	
ZARITSKY magnitude *(error)*	U = 17.035 *(0.068)*	B = 15.953 *(0.046)*	V = 14.587 *(0.02)*	I = 12.989 *(0.078)*
AKARI IRC flux [Jansky] *(error)*	S09 = 0.3021 *(0.0097)*		S18 = 0.3096 *(0.0299)*	
MSX6C flux [Jansky] *(quality flag)*	A	C	D	E
IRAS flux [Jansky] *(quality flag)*	Fnu12 = 0.277 *(3)*	Fnu25 = 0.357 *(3)*	Fnu60 = 0.4 *(1)*	Fnu100 = 1 *(1)*
FIRAS flux [Jansky] *(quality flag)*	Fnu12 = 0.322 *(3)*	Fnu25 = 0.308 *(3)*	Fnu60 = 0.307 *(1)*	Fnu100 = 1.02 *(1)*
MIPS magnitude *(quality flag)*	24um = 3.547 *(0.008)*		70um = 2.516 *(0.027)*	

Spectroscopic data

ISO TDT	
IRAS LRS	
SPITZER	009.248-74.331.dat

Fig. 1. Example of the screen shown for a selected object from the SMC catalogue (IRAS 00350-7436).

For the MCs objects we find the counterpart sources in the SAGE[3] survey of the LMC (Meixner et al. 2006) and the SAGE-SMC survey (Gordon et al. 2011). The SAGE surveys give photometry in the four filters (3.6, 4.5, 5.8, and 8 μm) from the IRAC instrument as well as in 24 and 70 μm (there is also the 160 μm filter but we have not noticed any detection) bands from the MIPS[4] photometer on board *Spitzer*. Using the IRAC coordinates as the reference positions, we searched several additional catalogues for the photometric data. However, searching in the radius of 5″we have not found the counterparts in the SAGE catalogue for eight objects in the LMC (IRAS F04353-6702, IRAS 04375-7247, IRAS F04537-6509, SMP LMC 61, SMP LMC 79, IRAS F06108-7045, IRAS 06111-7023, and SMP LMC 99). Therefore we used 2MASS coordinates to find the counterparts for them. In the optical range we gathered information from the MCPS[5] of the LMC (Zaritsky et al. 2004) and SMC (Zaritsky et al. 2002) in the *U*, *B*, *V* and *I* filters. Near- and mid-IR photometry consist of a few surveys: 2MASS (Skrutskie et al. 2006) and 2MASS-6X (*J*, *H*, and K_s filters for both surveys) which covered the MCs with longer exposure times (Cutri et al. 2006), WISE[6] (Wright et al. 2010), which provides observations in W1 (3.35 μm), W2 (4.6 μm), W3 (11.6 μm), and W4 (22.1 μm) filters, MSX6C[7] point source catalogue (Egan et al. 2003) from which we used *A*, *C*, *D*, *E* filters (8.28, 12.13, 14.65, and 21.34, respectively), and AKARI[8] IRC survey (9 and 18 μm bands; Ishihara et al. 2010). We assembled additional data from the IRAS[9] catalogue (Helou & Walker 1988) of point sources and its deeper edition FIRAS[10] (12, 25, 60, and 100 μm bands for both surveys; Moshir 1990). The photometry for the MIPS 70 μm band was available for only two objects in the SMC and nine objects in the LMC, whereas for the IRAS/FIRAS 60/100 μm band for only one object in the SMC, and four objects in the LMC.

In the case of Galactic objects (and Sgr dSph ones) we have used the 2MASS coordinates as the reference positions and added the data from a few additional catalogues. However, in the case of IRAS 15531-5704 we could not find the counterpart in the 2MASS catalogue in the radius of 2″, thus the WISE coordinates were used as the reference. The third release of the DENIS[11] catalogue (The Denis Consortium 2005) gives similar spectral coverage as 2MASS: I, J, and K_s. The first edition

[3] SAGE: Surveying the Agents of Galaxy Evolution.
[4] MIPS: Multiband Imaging Photometer for *Spitzer*.
[5] MCPS: Magellanic Cloud Photometric Survey.
[6] WISE: Wide-field Infrared Survey Experiment.
[7] MSX6C: The Midcourse Space Experiment (version 2.3); 6C denotes data run using version 6.0 of convert software with the names of the sources based on the galactic positions.
[8] AKARI was the first Japanese astronomical satellite observing in the infrared range.
[9] IRAS: Infrared Astronomical Satellite.
[10] FIRAS: IRAS Faint Source Catalogue.
[11] DENIS: Deep Near Infrared Survey of the Southern Sky.

Table 2. Percentage of the collected photometric data for each of the catalogues.

	R	Sgr dSph [5]	SMC [22]	LMC [121]	Galactic [59]
	(arcsec)	(%)	(%)	(%)	(%)
MCPS (SMC)	5	0	77	0	0
MCPS (LMC)	5	0	0	82	0
GSC 2.3	2	80	0	0	86
DENIS	3	100	0	0	49
2MASS	2	100	95	86	98
2MASS 6X	2	0	95	91	0
SAGE-SMC IRAC	5	0	100	0	0
SAGE-LMC IRAC	5	0	0	93	0
GLIMPSE	5	0	0	0	3
MSX6C	5	0	36	68	49
WISE	5	100	95	96	100
AKARI IRC	5	100	50	92	100
AKARI FIS	10	0	0	0	56
IRAS	10	20	14	55	100
FIRAS	10	80	32	61	24
MIPS (24 μm)	10	0	95	92	0
MIPS (70 μm)	10	0	9	11	0

of the GLIMPSE[12] catalogue (Benjamin et al. 2003; Churchwell et al. 2009) provided coverage at 3.6, 4.5, 5.8, and 8 μm, but only for two objects from our sample. The optical photometry came from the GSC[13] catalogue (version 2.3.2; Lasker et al. 2008) and contains the data in Johnson B filter, and also B_j, V, F, N photographic filters. In a case of Galactic objects we found counterparts in the AKARI-FIS catalogue (Yamamura et al. 2010), which has the four bands at 65, 90, 140 (only two detections), and 160 μm (no detections).

The statistics in percentage of the collected photometric data for each of the catalogues is presented in Table 2. The first column contains the information about the search radius ($''$) used for each catalogue. The total number of objects in each galaxy is given in the square bracket. We note that the WISE survey provides the photometry for almost all sources.

All the catalogues consist of data that have been obtained from various epochs. In some variable sources the mismatch between the spectrum and the photometry is visible in the SED diagrams. This is clearly seen in the case of AGB stars, which are known to be the strong pulsators.

3. Spectral analysis

3.1. Manchester method

Our analysis is based on the "Manchester method", which was introduced by Zijlstra et al. (2006) for mass-losing carbon stars in the LMC and by Sloan et al. (2006) for mass-losing carbon stars in the SMC. It uses two colour indices, [6.4]−[9.3] and [16.5]−[21.5], from which the former correlates with optical depth, while the latter serves for determination of the colour temperature, which we considered as the derived dust temperature (T_d). The [6.4]−[9.3] colour is calculated from the *Spitzer* spectra using separate flux integrations from 6.25 to 6.55 μm and from 9.1 to 9.5 μm. We summed over the regions 16–17 μm and 21–22 μm to simulate the second colour value. This method was also used by Sloan et al. (2016) to model the continua for the carbon-rich stars in the MCs. We followed their recipe to get the continuum level in each spectrum (with a modification for the post-AGB objects and a few PNe).

[12] GLIMPSE: Galactic Legacy Infrared Mid-Plane Survey Extraordinaire.
[13] GSC: the Guide Star Catalogue.

Table 3. List of [14.95]−[21.5] colour values for the PNe with the 16–18 μm feature.

Name	[14.95]−[21.5] (mag)
PN K 3-60	1.618 ± 0.005
SMP LMC 79	...
SMP LMC 78	...
SMP LMC 75	1.407 ± 0.009
SMP LMC 71	1.722 ± 0.018
SMP LMC 61	1.145 ± 0.009
SMP LMC 38	1.453 ± 0.015
SMP LMC 36	1.349 ± 0.008
SMP SMC 17	1.611 ± 0.009

We used this method in its original form for the carbon-rich AGB objects and PNe. However, the range between 21 and 22 μm in the *Spitzer* spectra of PNe is not completely free from nebular lines. In this spectral region the [Ar III] forbidden line at 21.83 μm can appear. Another transition of the [Ar III] line is visible at 8.99 μm. We have checked all the PNe spectra in our sample for presence of both [Ar III] lines, but only a very weak [Ar III] line at 8.99 μm has been found.

Moreover, in the spectra of nine PNe with strong polycyclic aromatic hydrocarbons (PAHs), we found the new detections of an unidentified emission feature between about 16 and 18 μm (hereafter the 16–18 μm feature), which might be attributed to PAHs (Peeters et al. 2004; Boersma et al. 2010). The spectra in the 5–20.5 μm range for those objects are shown in Fig. 2. For this group of objects we changed the shorter side of [16.5]−[21.5] colour and integrated flux from 14.8 to 15.1 μm. We note that the values of this new [14.95]−[21.5] colour are given in Table 3.

However, in the spectra of SMP LMC 78 and SMP LMC 79 the 16–24 μm feature is also visible (see Fig. 8 and the related discussion below), and the [14.95]−[21.5] colour is affected by this feature. Therefore, we removed these objects from further analysis, and did not report their [14.95]−[21.5] colour. The names of those objects are given in bold face in Table 3.

In the case of post-AGB stars we redefined the colour indices, depending on the strength of the 21 μm feature. Generally, if the 21 μm band is not visible or is weak (group I) we used the [18.4]−[22.45] colour (summing the flux from 18.1 to 18.7 and 22.3 to 22.6 μm). When the 21 μm feature is relatively strong (group II) we took the [18.4]−[22.75] colour (summing the flux from 18.1 to 18.7 and 22.5 to 23 μm). For objects with a very strong 21 μm feature (group III) we used the [17.95]−[23.2] colour (summing the flux from 17.8 to 18.1 and 23 to 23.4 μm).

The [6.4]−[9.3] colour has been defined in the Manchester method on the basis that those spectral ranges represent the continuum level of carbon-rich AGB stars. However, for post-AGB objects and PNe this colour overlaps with the PAH band at 6.2 μm. Therefore we defined a new [5.8]−[9.3] colour, which is similar to the [6.4]−[9.3] one, but avoids the 6.2 μm band, and other spectral features such as the [Mg V] line at 5.61 μm. The short wavelength part of this colour was constructed by summing the flux from 5.7 to 5.9 μm, whereas we kept the long wavelength part of the colour in its original form.

Table 4. List of colour indices used in this work.

Colour index	Left int. (μm)	Right int. (μm)	Cont. fit. range (μm)	#AGB	#Post-AGB	#PNe
[6.4]−[9.3]	6.25–6.55	9.1–9.5	...	112	0	0
[5.8]−[9.3]	5.7–5.9	9.1–9.5	...	0	35	50
[16.5]−[21.5]	16–17	21–22	16–22, 20–23	112	0	42
[14.95]−[21.5]	14.8–15.1	21–22	20–23	0	0	7 [(a)]
[18.4]−[22.45]	18.1–18.7	22.3–22.6	20–23	0	22 [(b)]	0
[18.4]−[22.75]	18.1–18.7	22.5–23	18.5–19	0	10 [(c)]	0
[17.95]−[23.2]	17.8–18.1	23–23.4	18–18.5	0	11 [(d)]	0

Notes. The table lists: name of the colour, left and right integration range, continuum fit range, and number of objects for which such the colour was obtained. [(a)]Sources with the 16–18 μm feature. [(b)]Weak or not present 21 μm feature. [(c)]Relatively strong 21 μm feature. [(d)]Strong 21 μm feature.

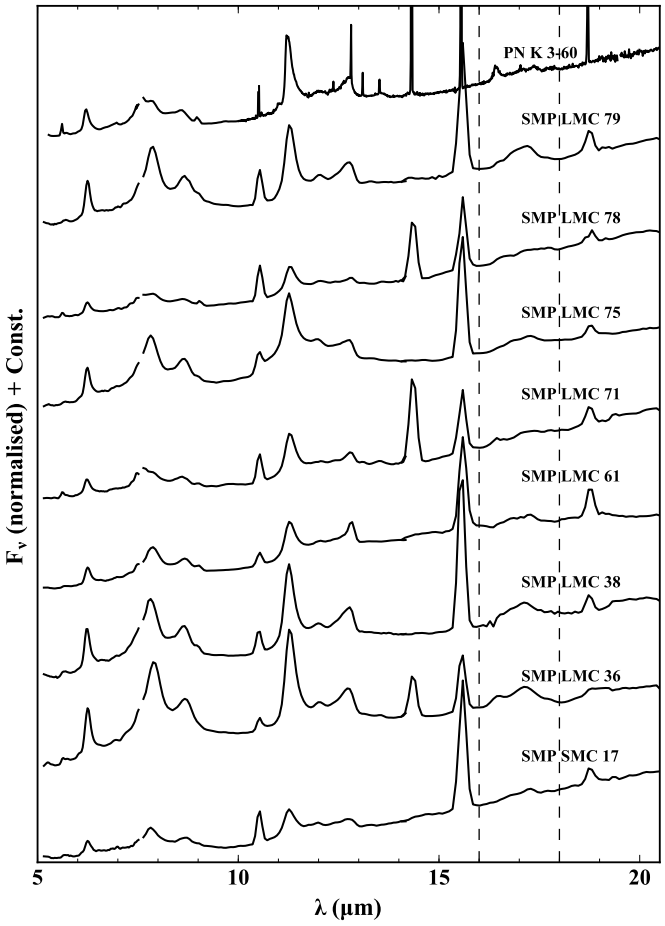

Fig. 2. 5–20.5 μm spectra for objects showing the 16–18 μm emission feature (solid lines). These spectra are normalised to the flux density at 18 μm. The names of objects are shown above the spectra. The spectrum of PN K3-60 was partially obtained using low (SL) and high-resolution (SH/LH) modes. The region containing this feature is shown by the dashed vertical lines.

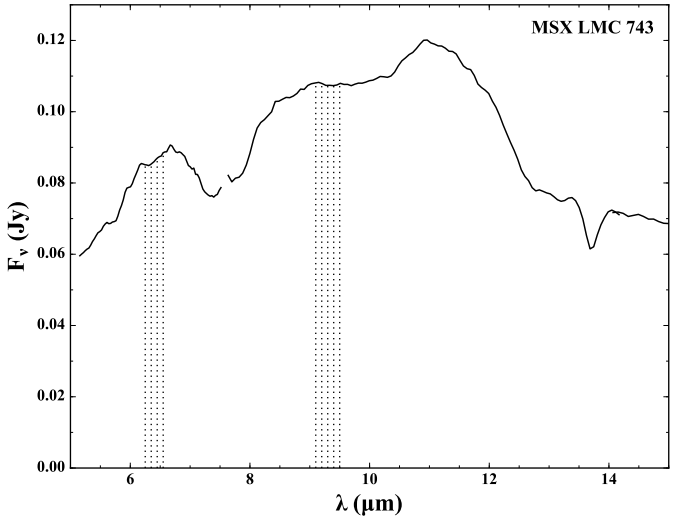

Fig. 3. Manchester method applied to the shorter part of the spectrum of MSX LMC 743 (solid line). The dotted areas show the ranges used to determine the [6.4]−[9.3] colour.

The list of all colour indices that have been used in this work is shown in Table 4. It contains the name of colour index, the short and long wavelength integration ranges, the range of the continuum fit, and number of objects for which such a colour index was calculated (among AGBs, post-AGBs, and PNe).

To model the continuum under the 30 μm feature we used a black-body function with the derived dust temperature and fitted its continuum level to the selected wavelength ranges that depend on the kind of the object. For the AGB stars, we applied the same fitting range as Sloan et al. (2016): 16–22 μm, whereas for the PNe we used 20–23 μm. The fitting range for the post-AGB objects is different for each of the three groups above: 20–23 for the group I, 18.5–19.0 for the group II, and 18–18.5 μm for the group III. There are 22 carbon-rich post-AGB objects in the group I (one SMC, 11 LMC, and ten Galactic objects), ten in the group II (one SMC, two LMC, and seven Galactic objects) and 11 in the group III (one SMC, four LMC, and six Galactic objects).

Figures 3 and 4 show how the Manchester method works in its original form for the shorter and longer part of the spectrum, respectively. As an example we used the carbon star MSX LMC 743. Figure 5 shows examples of the fitted continuum for a carbon-rich AGB star (IRAS 05113-6739) at the top panel and a carbon-rich PN (Hen 2-5) on the bottom panel. In Fig. 6 we show examples of the fitted continuum for each of three groups of post-AGB objects: 2MASS J05122821-6907556 from group I at the top panel, IRAS F05110-6616 from group II in the middle panel, and SAGE J052520-705007 from group III in the bottom panel. We note how the strength of the 21 μm feature is increasing from the group I to III.

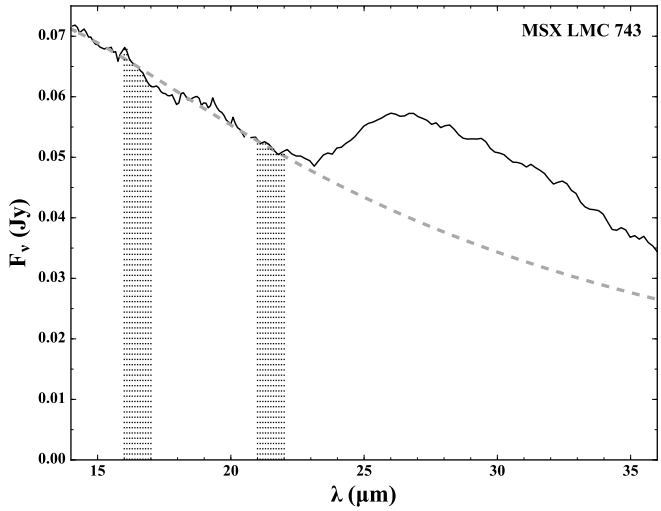

Fig. 4. Manchester method applied to the longer part of the spectrum of MSX LMC 743 (solid line). The dotted areas show the ranges used to determine the [16.5]−[21.5] colour, and serves for estimation of the colour temperature. The dashed grey line represents the continuum under the 30 μm feature.

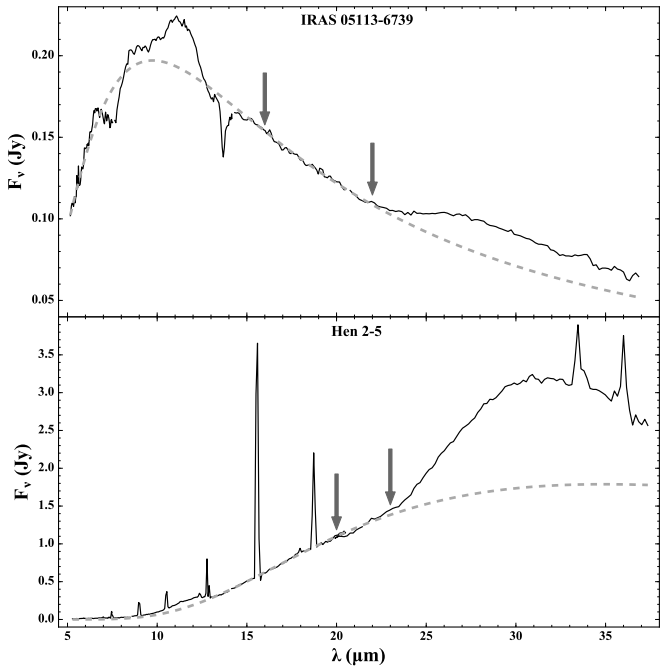

Fig. 5. Examples of the fitted continuum for a carbon-rich AGB star (*top*) and a PN (*bottom*). Spectra are drawn in black solid lines, while the grey dashed lines show the fitted black-body with a single temperature derived from the [16.5]−[21.5] colour. The arrows indicate the spectral ranges to which the blackbodies are fitted. The names of the objects are shown in the upper-central part of each panel.

Despite the Manchester method being a very useful tool for a uniform analysis of big samples of carbon-rich stars, we noticed that its usage is limited for some AGBs and post-AGBs with 21 μm feature. We were unable to obtain black-body fits for a total 33 objects (18 AGB stars and 15 post-AGB objects). The objects with bad fits were removed from the further analysis, and only the values of the Manchester colours are presented in Tables 1, 5, and D.1–D.6. They are also distinguished by names in bold face.

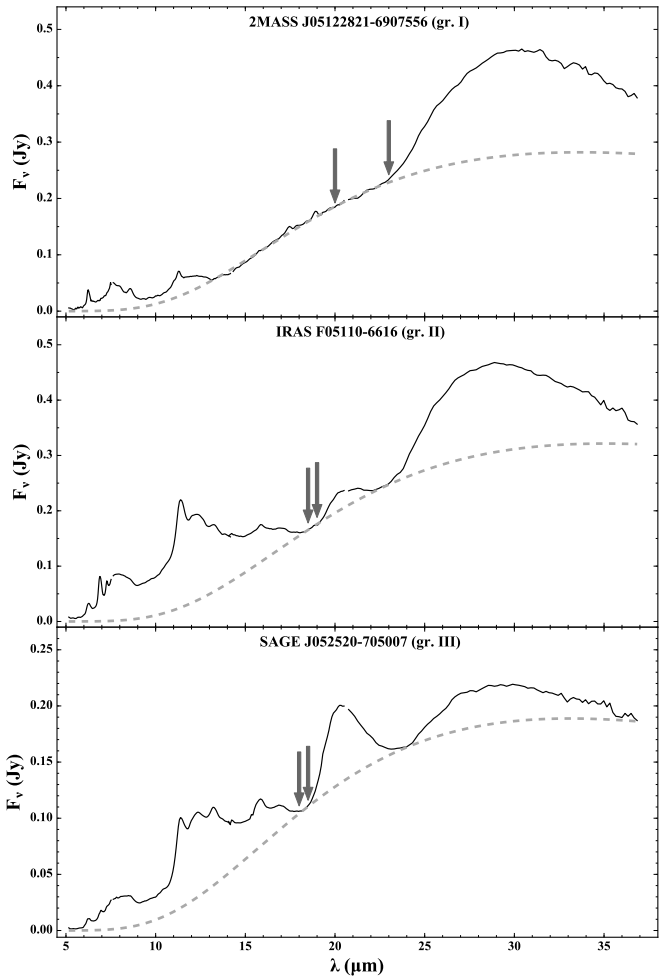

Fig. 6. Examples of the fitted continuum for the post-AGB objects from the group I to III (starting from the top). Spectra are drawn in black solid lines, while the grey dashed lines show the fitted black-body with a single temperature. The arrows indicate the spectral ranges to which the blackbodies are fitted. The names of the objects are shown in the upper-central part of each panel.

The problems with modelling the continuum can be divided into four categories, which are presented in Fig. 7. The top panel of Fig. 7 shows the case in which the shape of the 16–22 μm continuum causes the wrong determination of the $T_{\rm d}$. There are 11 such objects of which ten are AGB stars (all in the LMC), and the remaining star is a post-AGB object without the 21 μm feature (IRAS 00350-7436 from the SMC). The second panel of Fig. 7 presents an example of an object for which the obtained value of $T_{\rm d}$ is too high. For five objects we observe such a problem (one in the SMC, three in the LMC, and one in the Milky Way). The third panel of Fig. 7 shows the problem of modelling the continuum for some post-AGB objects. The explanation of this behaviour may lie in the fact that one of the ranges used for obtaining $T_{\rm d}$ is taken from the region between the 21 and 30 μm features. When the 21 μm feature is strong, this region might be bumped up, and causes too low the $T_{\rm d}$ value. There are 12 such objects (one in the LMC and 11 in the Milky Way). The bottom panel shows that in some cases the Manchester Method may lead to the reduction of the obtained flux of the 30 μm feature. We notice this for three objects (all in the LMC): MSX LMC 1400 which serves as the example, 2MASS J05102834-6844313, and IRAS 05568-6753. In the second object the continuum bisects the profile of the 30 μm feature.

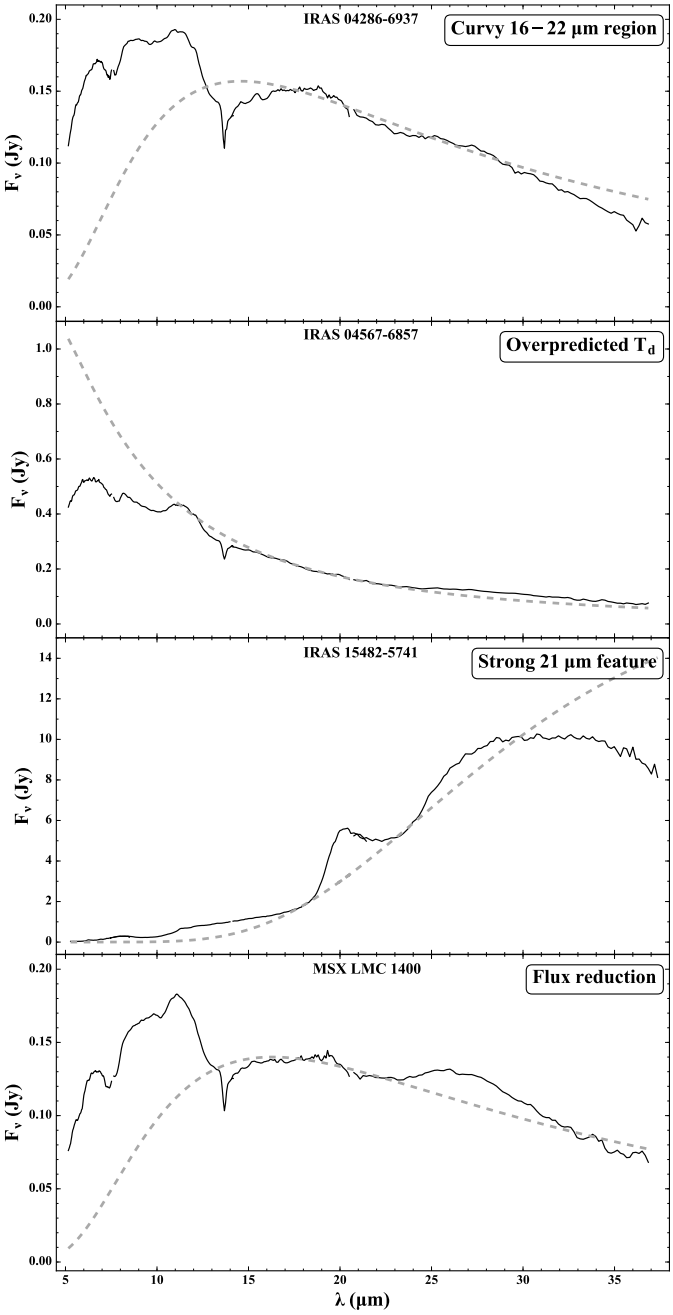

Fig. 7. Examples of the bad continuum fits to the spectra showing the constraints of the Manchester method. The spectra are drawn in black solid lines, while the grey dashed lines show the fitted black-body with a single temperature. The names of the objects are shown in the upper-central part of each panel.

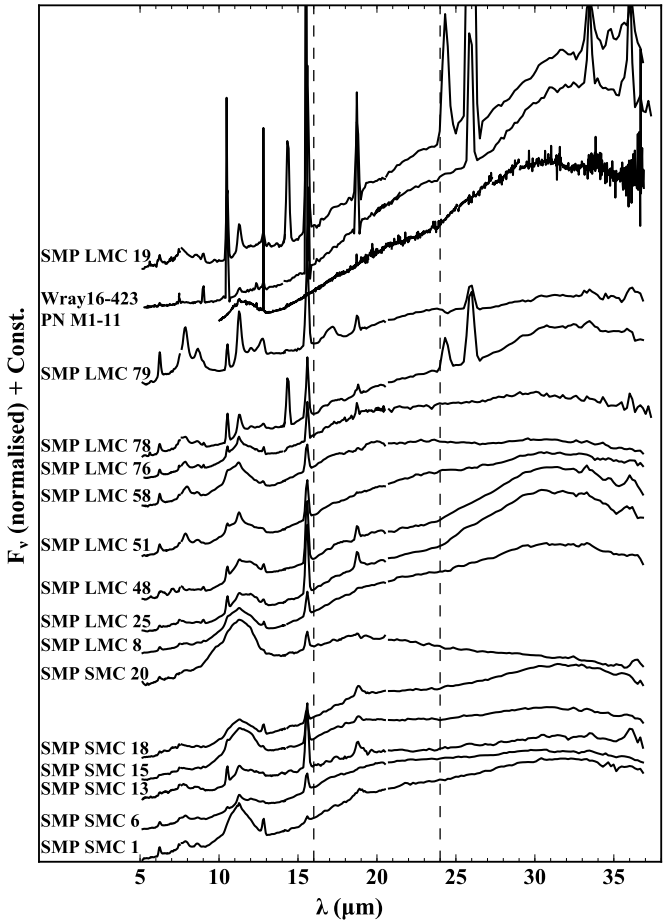

Fig. 8. PNe excluded from analysed sample, because of presence of the broad emission feature, which is typically visible around 16–24 μm. The spectra (solid lines) are normalised to the flux density at 16 μm and offset for clarity. The names of the objects are shown above the spectra.

Two post-AGB objects with bad fits are not in these four categories (both from the group I). In the *Spitzer* spectrum of the first object, IRAS 19477+2401, the SH part of the spectrum is very noisy, and a big jump between the SH and LH segments is visible. These two facts cause that the determination of the continuum is uncertain. In a case of IRAS 15531-5704, the 20–23 μm region of spectrum where the continuum is fitted, contains a curvy bump. This results in an overprediction of the continuum.

We excluded 17 additional PNe from the analysis, because of the presence of an unidentified broad emission feature between ~16–24 μm (in some cases this feature can extends beyond 24 μm), which affects the values of the [16.5]−[21.5] colour. In these cases we only have reported the values of the [5.8]−[9.3] colour. Six out of these 17 objects (SMP SMC 1, 6, and SMP LMC 8, 58, 76, 78) have been already referred to by Bernard-Salas et al. (2009) as "Bump16" sources with a broad excess between 16–22 μm. García-Hernández et al. (2012) found this feature in another six MCs PNe that are in our sample (SMP SMC 13, 15, 18, 20, and SMP LMC 25 and 48). The carrier of this unusual dust feature remains unclear. Otsuka (2015) reported the presence of this feature in the Sgr dSph planetary nebula Wray-16-423, and called it the broad "16–24 μm feature". In our work we follow their nomenclature. In addition, the authors also confirmed the presence of the 16–24 μm feature in SMP LMC 19. In our Galaxy, Otsuka et al. (2013) found this feature in the fullerene-containing planetary nebula PN M1-11 and PN M1-12. Nevertheless, the presence of this feature in the spectrum of PN M1-12 is not obvious to us, thus we have not removed it from the further analysis in our work. Moreover, the presence of this spectral feature is indicated by the question mark in Table D.3. During our analysis, we made the first detections of the 16–24 μm feature in the *Spitzer* spectrum of SMP LMC 51 and 79. The spectra of all the PNe showing the 16–24 μm feature are presented in Fig. 8. Their names are also given in bold face in Tables 1, 5, and D.1–D.6.

The 16–24 μm feature has been discovered in the carbon-rich post-AGB objects as well. The first detection was made by

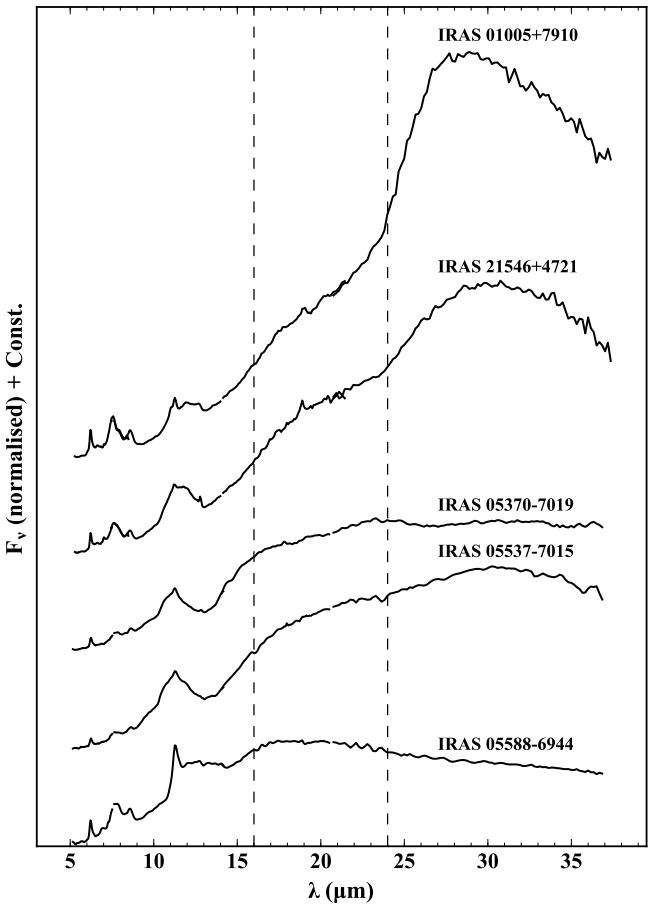

Fig. 9. Post-AGB objects excluded from analysed sample, because of the broad emission feature presence, which is typically visible around 16–24 μm. The spectra (solid lines) are normalised to the flux density at 16 μm and offset for clarity. The names of the objects are shown above the spectra.

Zhang et al. (2010) in the *Spitzer* spectrum of IRAS 01005+7910. Matsuura et al. (2014) found this feature in the LMC post-AGB object IRAS 05588-6944. We also noticed very similar feature in the *Spitzer* spectra of IRAS 05370-7019, IRAS 05537-7015, and IRAS 21546+4721 for the first time. They are analysed by Sloan et al. (2014) and included to the group called "big-11", because they show a strong 11.3 μm feature. We excluded these five post-AGB objects from the further analysis, and marked them also by the bold face names in Tables 1, 5, and D.1–D.6 as in a case of the PNe with the 16–24 μm feature. The spectra of these post-AGBs are shown in Fig. 9.

3.2. Strength and central wavelength of the 30 μm feature

The 30 μm band is present between 24 and 45 μm (Otsuka et al. 2014). The long wavelength side of this feature is beyond the end of the *Spitzer* spectral coverage, thus it is not possible to estimate the full emission of the feature. Therefore, we extrapolated the black-body continuum on the short wavelength side of the 30 μm feature only. We measured the strength of the feature F/Cont (30 μm), which is a ratio of the integrated flux from 24 to 36 μm above the continuum, divided by the integrated underlying continuum for the same spectral range. We applied the same range of the integration for the AGB objects as well as post-AGB stars and PNe to be in agreement with Sloan et al. (2016) results. For the PNe we removed the forbidden emission lines of [Ne V] at 24.32 μm, [O IV] at 25.89 μm, [S III] at 33.48 μm, and [Ne III] at 36.01 μm, when they were visible, before measuring the strength of the 30 μm feature. In addition, we determined the central wavelength (λ_c) of the 30 μm feature. This central wavelength is defined as the wavelength at which (after the subtraction of the continuum), the flux on the both sides is equal.

Table 5 lists the results of the spectroscopic analysis for the objects in the Sgr dSph. Appendix D presents the Tables D.4–D.6 with the spectroscopic results for the SMC, LMC, and Milky Way. In each of these Tables we present the names of the objects, the colours derived from the Manchester method and its modifications ([5.8]−[9.3], [6.4]−[9.3], [16.5]−[21.5], [18.4]−[22.45], [18.4]−[22.75], and [17.95]−[23.2]) as well as the derived dust temperatures (T_d). Table 5 contains no post-AGB objects, but we keep the columns with the colours intended for those objects with an aim of providing the same structure in all of the Tables. Finally, we present the calculated central wavelength (λ_c), and the strength of the 30 μm feature, F/Cont. Usually, the profile of the 30 μm feature rises starting from 24 μm, and after reaching the maximum it turns down at the long-wavelength cut-off. If this decline is not visible in the spectrum, then we assumed that the 30 μm feature is somehow contaminated or not present in the spectrum, and we do not treat such an object as the true 30 μm source. Basically, we repeated the values of the [6.4]−[9.3] colour, [16.5]−[21.5] colour, and F/Cont together with their errors for the carbon-rich AGB stars in the SMC and LMC from Sloan et al. (2016) (see their Table 5 in the online content). However, Table 5 and Tables D.4–D.6 were supplemented by the additional parameters of the 30 μm feature like the T_d and λ_c. On the other hand, in a few cases the results given by Sloan et al. (2016) seemed to be unrealistic, and we have not included them in our tables with the results. Below we present the arguments for these changes.

We have not shown the results of the F/Cont (30 μm) for two objects from their SMC list: MSX SMC 036 and MSX SMC 054. The values of the T_d and λ_c (additional parameters given by us) have not been shown for them as well. In a case of MSX SMC 036, the authors reported the value of the F/Cont about 0.3. We decided to remove it from our sample on the grounds that the profile of the feature was not turning down at the long-wavelength *Spitzer* cut-off in the both used databases of *Spitzer* spectra. In a case of the second object, MSX SMC 054, the authors reported the value of F/Cont ~0.2, but the maximum of the continuum was above the *Spitzer* spectrum, which indicated that the obtained T_d is too high (bad fit of continuum). We marked this object in bold face in Tables D.1 and D.4. The example of spectrum with such the problem is shown in the second panel (from the top) of Fig. 7.

We find the differences in the profiles of the 30 μm feature in the two databases of spectra we have used (*Spitzer*; Sloan et al. 2016, and the CASSIS) for three LMC objects: OGLE J051306, MSX LMC 782, and MSX LMC 787, as follows. For the first object, OGLE J051306, the authors reported the value of the F/Cont ~0.7, but the profile of the feature was not turning down at the end of the spectrum (like in a case of MSX SMC 036 in the SMC). On the other hand, the CASSIS spectrum of this object has not shown any rise behind 24 μm, indicating that we were not dealing with the true 30 μm source. In the end, this object was removed from the analysed sample.

The situation of MSX LMC 782, MSX LMC 787 was more difficult. Their *Spitzer* spectra from Sloan et al. (2016) are shown by the solid lines in Fig. 10. The top panel contains the spectrum of MSX LMC 782, whereas in the bottom panel we show the spectrum of MSX LMC 787. The authors reported the

Table 5. Spectroscopic results for the Sgr dSph objects.

Target	[5.8]−[9.3] (mag)	[6.4]−[9.3] (mag)	[16.5]−[21.5] (mag)	[18.4]−[22.45] (mag)	[18.4]−[22.75] (mag)	[17.95]−[23.2] (mag)	T_d (K)	λ_c (30 μm) (μm)	F/Cont (30 μm)
Sgr 3	...	0.554 ± 0.006	0.327 ± 0.012	...	...	...	436 ± 13	28.978 ± 0.111	0.390 ± 0.014
Sgr 7	...	0.763 ± 0.004	0.209 ± 0.012	...	...	...	645 ± 31	29.326 ± 0.228	0.195 ± 0.014
Sgr 15	...	0.505 ± 0.005	0.201 ± 0.013	...	...	...	669 ± 36	29.338 ± 0.194	0.165 ± 0.015
Sgr 18	...	0.818 ± 0.003	0.208 ± 0.011	...	...	...	650 ± 28	29.175 ± 0.136	0.243 ± 0.013
Wray16-423	2.287 ± 0.086	...	...	...	...	...	...	...	...

Notes. The table lists: names, six colours, dust temperature (T_d), central wavelength (λ_c), and strength of the 30 μm feature (F/Cont). The tables with the Galactic and MCs objects are available in Appendix D.

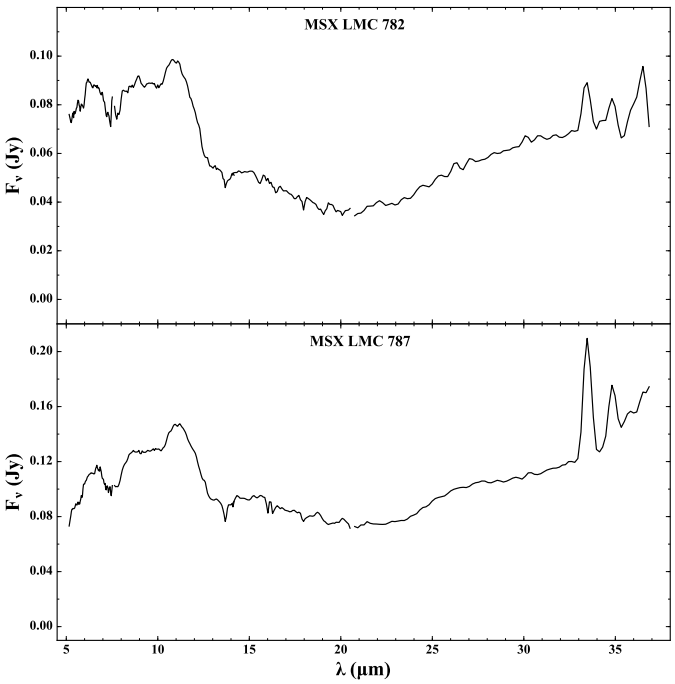

Fig. 10. Spectra of MSX LMC 782 (*top*), and MSX LMC 787 (*bottom*), showing the problem with calibration. The *Spitzer* spectra are represented by solid lines.

values of the F/Cont of about 1.4 for MSX LMC 782 and 1.1 for MSX LMC 787. The spectra from Sloan et al. (2016) have shown the steep rise starting from around 23 μm, and no decline up to the end of the spectra. From this point of view, these objects should have been removed from the analysed sample. However, the CASSIS spectra have shown a clear decline, therefore, we have kept them as the true 30 μm sources. These spectra are clearly affected by nearby background emission. The extraction method for the CASSIS spectra was more effective in removing that background than our method, because it added the step of fitting the background and separating it from the extracted spectrum of the source. Because of this problem the values of the λ_c and F/Cont were not shown by us in Table D.5, but we kept the T_d.

In addition, we did not show results for another 18 objects from the Sloan et al. (2016) LMC list (their names are given in bold face in Tables D.2 and D.5, except for one object – MSX LMC 974), whereas in three cases the different values have been reported by us (IRAS 05416-6906, MSX LMC 494, and IRAS 05026-6809). Below we describe the reasons of these changes.

The *Spitzer* spectrum of MSX LMC 783 has not shown any signs of decline behind 24 μm. The CASSIS spectrum has had the same trend, thus we removed it from our sample. The authors have reported the value of the F/Cont of about 0.3.

In a case of MSX LMC 974 the weak 30 μm feature has been observed, whereas the authors reported the value of the F/Cont ~0.2. This value is overestimated, just as value of λ_c (>33 μm), because we noticed that the *Spitzer* spectrum is very noisy over 32 μm, giving the additional emission to the end of spectrum. We report only the T_d value for this object.

In the *Spitzer* spectra of ten LMC objects (IRAS 04286-6937, IRAS 05010-6739, IRAS 05103-6959, IRAS 05107-6953, MSX LMC 220, IRAS 05446-6945, and LI-LMC 1758, IRAS 04374-6831, IRAS 04473-6829, MSX LMC 218), the negative (or positive but close to 0) values of the F/Cont were observed. The closer look into their *Spitzer* spectra has shown they have the 30 μm feature, but the continuum obtained for them is not correct. It is caused by the curved shape of the spectrum in the region from which the Manchester colours were taken to determine the T_d. The exemplary spectrum showing this kind of the bad continuum fit is shown in the top panel of Fig. 7 for IRAS 04286-6937.

In the *Spitzer* spectra of MSX LMC 1400, 2MASS J05102834, and IRAS 05568-6753 we noticed the reduction of the obtained flux of the 30 μm feature. The maximum of the black-body continuum in IRAS F04537-6509, IRAS 04567-6857, and MSX LMC 92 was above the spectrum, which indicated that the value of the T_d was overestimated (like for MSX SMC 054 in the SMC; see above).

In the *Spitzer* spectrum of carbon-rich AGB object IRAS 05416-6906, the [Ar III] at 21.83 μm and [S III] lines at 18.71/33.48 μm were observed. The classification of this object as carbon-rich AGB star, was made by Woods et al. (2011). Neugent et al. (2012) described IRAS 05416-6906 as the yellow supergiant (YSG) with the spectral type of B2.5Ia, which was determined by Fitzpatrick (1991). The presence of this emission lines may suggest that this is a binary carbon-rich AGB star with a hot companion. We deleted these lines before measuring the value of the F/Cont. After removal of the nebular lines we should have expected the increase of the F/Cont. Meanwhile, the value of the F/Cont, which has been obtained by us is about 6% larger than the value reported by Sloan et al. (2016). This was caused by the fact that the value of the [16.5]−[21.5] colour has changed after the removal of [Ar III] line, giving the bigger value of the F/Cont.

Finally, we decided to add two objects for which the values of the F/Cont were not given by Sloan et al. (2016): MSX LMC 494 and IRAS 05026-6809. This was made on the grounds that the 30 μm feature is well visible in their *Spitzer* spectra, and the

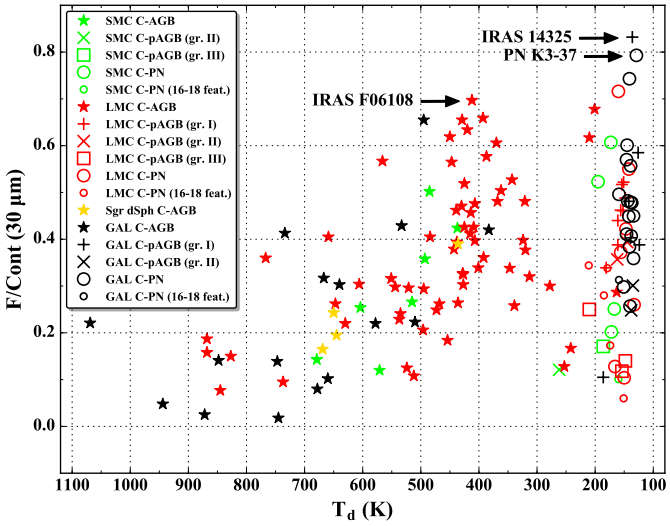

Fig. 11. Strength of the feature as a function of the dust temperature.

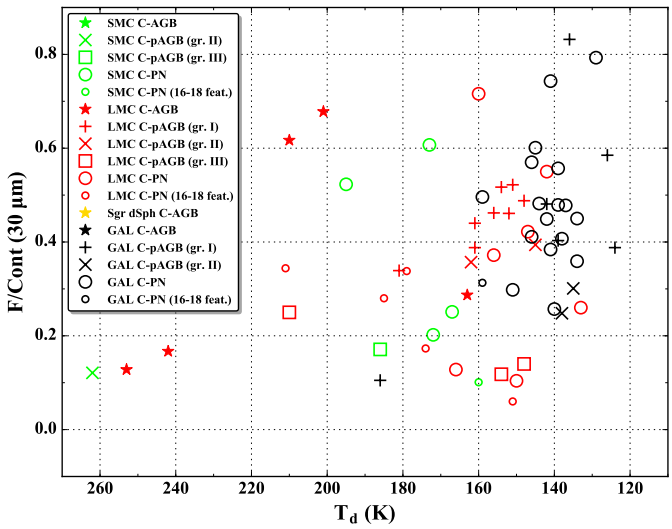

Fig. 12. Strength of the feature as a function of the dust temperature – zoom for the region of the objects with the coldest dust.

decline in the spectrum was observed – also in the CASSIS spectra.

4. Results and summary

4.1. Relations between obtained parameters

Altogether, we are able to determine all parameters of the 30 μm feature for 42 Galactic objects (16 AGB stars, six post-AGB stars in group I, two post-AGBs in gr. II, and 18 PNe); 89 LMC objects (64 AGB stars, eight post-AGB stars in gr. I, two post-AGBs in gr. II, three post-AGBs in gr. III, and 12 PNe); 14 SMC objects (seven AGB stars, one post-AGB star in gr. II and III, and five PNe); four Sgr dSph objects (AGB stars). In Fig. 11 we show the strength of the 30 μm feature as a function of the $T_{\rm d}$. The horizontal axis is presented reversely to show the evolution of carbon-rich objects from the AGBs up to PNe. We also distinguish the group of the PNe with the 16–18 μm feature, which has been discussed in Sect. 3.1. These PNe are represented as small open circles.

The strength of the feature clearly increases as $T_{\rm d}$ decreases to about 400 K. After that, the large mass-loss rate and probably the resulting self-absorption reduces the strength of the 30 μm feature. During the post-AGB phase, when the intense mass-loss has terminated, the optical depth of the circumstellar envelope is smaller, and the feature is visible again, becoming comparable in the strength to the strongest feature in AGB stars with $T_{\rm d}$ between 300 and about 500 K. In our sample AGB stars in this region of $T_{\rm d}$ are dominated by the LMC objects. However, the Galactic sample from Sloan et al. (2016), which is based on the ISO spectra, extends much further in the F/Cont than our Galactic sample (see their Fig. 6). Their three Galactic objects have F/Cont between 0.7 and 0.9. Without unrealistic results for two LMC objects discussed in Sect. 3.2 (MSX LMC 782 and MSX LMC 787), their Galactic sources compose a group with the strongest 30 μm feature. The strongest 30 μm feature in our sample was derived for IRAS F06108-7045 in case of AGB stars, IRAS 14325-6428 among the post-AGB objects, and PN K3-37 in PNe. These objects are marked by the black arrows, and abbreviations of their names in Fig. 11.

In Fig. 12 we present the strength of the 30 μm feature as the function of the $T_{\rm d}$ between 110 and 270 K, to show the post-AGB objects and PNe more clearly. The symbols on the graph are the same as in Fig. 11. Despite the lack of correlation between the strength of the feature and $T_{\rm d}$, the Galactic post-AGB objects and PNe seems to have a slightly smaller $T_{\rm d}$ and larger strength of the feature in comparison with their counterparts from other galaxies. There are five carbon-rich AGB objects with 260 K > $T_{\rm d}$ > 160 K – all of them are the LMC members.

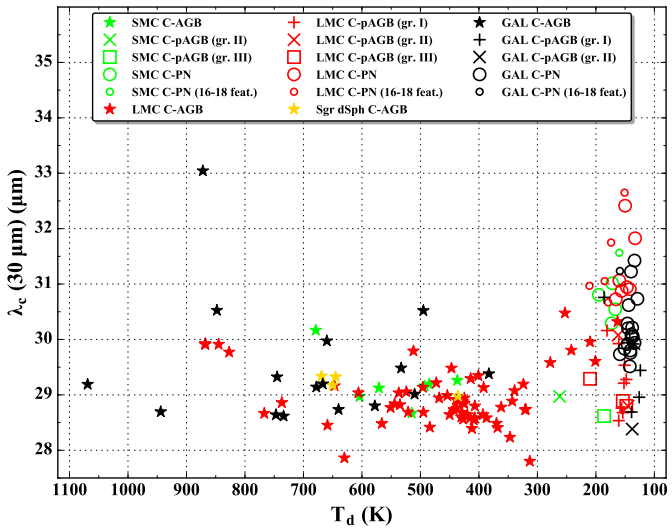

Fig. 13. Central wavelength as a function of the dust temperature.

Figure 13 shows the $\lambda_{\rm c}$ of the 30 μm feature as a function of the $T_{\rm d}$. The horizontal axis is reversed to show the evolutionary sequence from AGB stars, through post-AGBs up to PNe, and the symbols on the graph are the same as in Fig. 11. The $\lambda_{\rm c}$ seems to be independent with the changing $T_{\rm d}$. The majority of the carbon-rich AGB objects occupy the region of the $\lambda_{\rm c}$ between about 28.5 and 29.5 μm. However, some objects stick out from the main group. There are two objects (MSX LMC 950 and IRAS 06025-6712 – this one has the lower $T_{\rm d}$), which are located in the region, where the $\lambda_{\rm c}$ < 28 μm. In the spectra of these objects, the fitted continua are a little too high at the end of the spectra (in comparison with the other AGB objects), and thus result in the lower value of the $\lambda_{\rm c}$. Another interesting group of six LMC carbon-rich AGB objects occupies the region

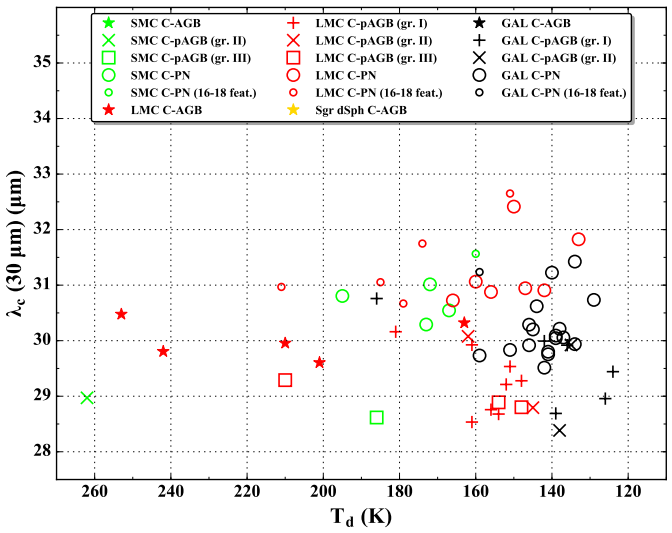

Fig. 14. Central wavelength as a function of the dust temperature – zoom for the region containing objects with the coldest dust.

Table 6. List of AGB objects from LMC with the coolest dust.

Name	T_d (K)	λ_c (30 μm) (μm)	Mass-loss rate ($M_\odot$ yr^{-1})	Mass-loss rate reference
IRAS 05509-6956	278 ± 3	29.58 ± 0.08	9.0×10^{-5}	(1)
IRAS 05026-6809	253 ± 3	30.48 ± 0.14	...	...
IRAS 05133-6937	242 ± 2	29.81 ± 0.22	8.9×10^{-5}	(1)
IRAS 05315-7145	210 ± 4	29.96 ± 0.04	1.7×10^{-4}	(1)
SHV 0528350-701014	201 ± 3	29.61 ± 0.10	...	...
IRAS 05495-7034	163 ± 2	30.32 ± 0.04	2.3×10^{-4}	(1)

Notes. The values of the T_d and λ_c are taken from Table D.5.
References. (1) Gruendl et al. (2008).

between 280 K > T_d > 160 K and 30.5 μm > λ_c > 29.5 μm (see Fig. 14 for more detailed view). The obtained by us T_d for those objects shows that their envelopes are cool. Four out of these six objects were classified by Gruendl et al. (2008) as "extremely red objects" (EROs). According to the authors, this class of objects is mainly characterised by extremely red mid-IR colours ([4.5]−[8.0] > 4.0), and none of them have counterparts in the 2MASS catalogue. The mass-loss rates obtained by Gruendl et al. (2008) for these four objects are between 8.9×10^{-5} and 2.3×10^{-4} $M_\odot$ yr^{-1}, which shows that they experience an intense mass-loss process. In Table 6 we list these objects in order of the decreasing T_d. First, the names of objects are presented, and then the T_d and λ_c from Table D.5 are shown. After that the values of the mass-loss rates with the corresponding reference are given.

There are ten carbon-rich AGB sources in the range of 900 K > T_d > 300 K and λ_c > 29.7 μm, which clearly stick out from the main group of the carbon-rich AGB stars. These objects are listed in Table 7 in order of the decreasing T_d. In the first column we present the names of the objects, and then the information about the host galaxy. After that the values of the T_d, λ_c, and F/Cont from Tables D.4–D.6 are repeated. In general, the 30 μm feature in these objects is weak, and then the λ_c might be not certain and shifted towards the longer wavelengths. The object showing the largest λ_c (>33 μm) in the analysed sample, IRAS 18120+4530, presents simultaneously the weakest value of F/Cont (~0.03). However, this is an artificial effect caused by

Table 7. List of AGB objects from Fig. 13, which are located in the region of 900 K > T_d > 300 K and 33.1 μm > λ_c > 29.7 μm.

Name	Location	T_d (K)	λ_c (30 μm) (μm)	F/Cont (30 μm)
IRAS 18120+4530 [a,b]	Milky Way	872 ± 57	33.04 ± 0.69	0.03 ± 0.01
IRAS 04433-7018 [a]	LMC	868 ± 78	29.93 ± 0.70	0.19 ± 0.02
OGLE J052242 [a,c]	LMC	868 ± 90	29.91 ± 0.99	0.16 ± 0.03
IRAS 16339-0317 [a]	Milky Way	848 ± 74	30.53 ± 0.19	0.14 ± 0.02
MSX LMC 1205 [a]	LMC	845 ± 62	29.91 ± 0.54	0.08 ± 0.02
MSX LMC 494 [a]	LMC	827 ± 64	29.77 ± 0.46	0.15 ± 0.02
MSX SMC 163 [a]	SMC	679 ± 31	30.17 ± 0.35	0.14 ± 0.01
IRAS 04188+0122 [a]	Milky Way	660 ± 26	29.97 ± 0.26	0.10 ± 0.01
MSX LMC 474 [a]	LMC	512 ± 17	29.79 ± 0.08	0.11 ± 0.01
IRAS 18384-3310 [d]	Milky Way	495 ± 12	30.52 ± 0.06	0.66 ± 0.01

Notes. The values of the T_d, λ_c, and F/Cont are taken from Tables D.4–D.6. [a]The 30 μm feature is weak. [b]The 30 μm feature is very weak. [c]Full name of object is OGLE J052242.09-691526.2. [d]The decline of the 30 μm feature after maximum is very slow.

the weakness of the 30 μm feature, and not a manifestation of any physical effect.

Figure 14 presents the λ_c of the 30 μm feature as the function of the T_d between 110 and 270 K, where the post-AGB objects and PNe are mostly visible. The symbols on the graph are the same as in Fig. 11. The main group of the post-AGB objects is located in the same range of λ_c as carbon-rich AGB stars – between 28.5 and 29.5 μm. However, there are eight post-AGB objects, which are located above this range and one Galactic post-AGB object a bit below at about 28.4 μm (IRAS 11339-6004). In addition, one post-AGB star, 2MASS J01054645-7147053 (gr. II, SMC) has the T_d = 262 K, and evidently sticks out from the main group. In case of PNe, the λ_c is clearly shifted towards the longer wavelengths. Hony et al. (2002) suggested that this is the effect of the temperature or a shape of the MgS dust grains. The most of the PNe are located in the range of the λ_c between about 29.5 and 31.5 μm. However, the Galactic PNe show rather the smaller values of the λ_c in comparison with the MCs PNe.

In the spectra of the PNe, which are located in Fig. 14 beyond the λ_c = 31.5 μm, the 30 μm feature starts to rise not from 24 μm as usual, but from 27 μm. These objects are (in order of increasing λ_c): SMP SMC 17 from the SMC, SMP LMC 38, 52, 99, 71 from the LMC. Moreover, the region between 24 and 27 μm in the *Spitzer* spectra of SMP LMC 52, SMP LMC 71 is additionally disrupted by presence of very strong [O IV] forbidden line at 25.89 μm, and relatively strong [Ne V] line at 24.32 μm. In the spectrum of SMP LMC 71, the [Ne V] line is roughly as strong as the [O IV] one. Their presence causes that the left edge of profile of the 30 μm feature may be disrupted, especially after removal of nebular lines. We note that in these cases, measuring values of the F/Cont and λ_c by integrating the flux from 24 to 36 μm leads to underestimated values of those parameters. Therefore, we have made the additional measurements of the F/Cont and λ_c, assuming the 27–36 μm integration range. This caused the increase in values of the F/Cont by 36–52%, whereas the change in the λ_c was no bigger than 0.8%.

Figure 15 consists of four panels, and shows some parameters as a function of the [6.4]−[9.3] colour for the carbon-rich AGB stars. Zijlstra et al. (2006) showed that the [6.4]−[9.3] colour provides a good estimate of the dust optical depth. In addition,

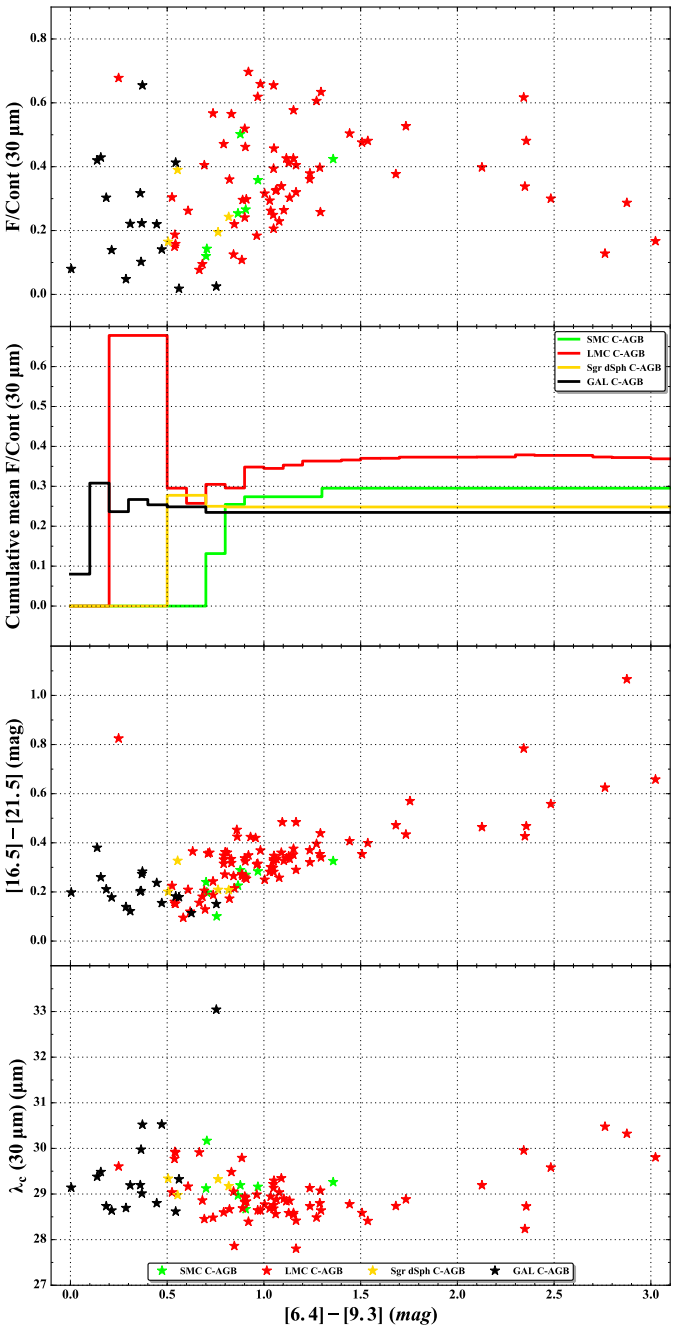

Fig. 15. *Top to bottom panels*: strength of the feature (F/Cont), cumulative mean of the F/Cont, [16.5]−[21.5] colour, and central wavelength (λ_c) as a function of the [6.4]−[9.3] colour.

the [6.4]−[9.3] colour shows a linear correlation with the measured mass-loss rates (Groenewegen et al. 2007). Symbols on the graph are in line with Fig. 11. However, the second panel (from the top) contains the cumulative distributions, presented by solid lines. Their colours are consistent with other panels.

The upper panel of Fig. 15 shows the F/Cont (30 μm) as a function of the [6.4]−[9.3] colour for the different populations of the carbon-rich AGB stars. The Galactic carbon-rich AGB stars in our sample are visible starting from about [6.4]−[9.3] ∼0 mag until 0.8 mag. However, our sample appears to be truncated by a selection bias against the redder objects. The Sloan et al. (2016) sample of Galactic objects based on the ISO is two times wider in the [6.4]–[9.3] colour, and it spreads from about 0 to 1.7 mag (see their Fig. 6). For the LMC population of objects, the first 30 μm emission is visible at the [6.4]−[9.3] = 0.25 mag (SHV 0528350-701014), and then the feature is not visible until the [6.4]−[9.3] colour is about 0.5 mag. SHV 0528350 is particularly red in the [16.5]−[21.5] colour. This object is the carbon-rich star with cool and detached dust shell (T_d = 201 K). The Sgr dSph objects also become visible from the [6.4]−[9.3] colour ∼0.5 mag, whereas in the SMC the first 30 μm emission is at about 0.7 mag. Basically, the formation of the 30 μm emission is clearly related to the metallicity of the hosted galaxy. In the metal-poor environments like the MCs, the 30 μm emission becomes visible for much redder [6.4]−[9.3] colours than in the Milky Way. The location of the Sgr dSph carbon-rich stars on this diagram indicates that the metallicity of this galaxy is similar to the LMC, or between the LMC and our Galaxy.

The second panel of Fig. 15 illustrates the cumulative mean of the F/Cont (30 μm) as a function of the [6.4]−[9.3] colour for the carbon-rich stars in the different galaxies. By solid lines we show the cumulative distribution with a step of 0.1 mag in the [6.4]−[9.3] colour. The cumulative distribution shows clearly how the 30 μm emission rises with the increasing [6.4]−[9.3] colour for the carbon-rich AGB stars in the different galaxies. In a case of the metal-poor galaxies, the much higher dust production rate and the cooler dust (see also the next panel) is needed to make the 30 μm emission visible. The plots for the Galactic and Sgr dSph objects become flat past the [6.4]−[9.3] colour of about 0.8 and 0.9 mag, respectively. In case of the SMC objects it happens past the [6.4]−[9.3] colour ∼1.4 mag. This is caused by the lack of the redder objects in the samples. Sloan et al. (2016) presented a similar cumulative plot, and their Galactic trace is above the MCs rising up to the ∼1.7 mag in the [6.4]−[9.3] colour, as has been already discussed in the upper panel.

The third panel of Fig. 15 presents the [16.5]−[21.5] colour as a function of the [6.4]−[9.3] colour. Zijlstra et al. (2006) showed that the [16.5]−[21.5] colour serves as an indicator of the dust temperature. The carbon-rich AGB stars form a linear sequence. However, the points are more dispersed for the [6.4]−[9.3] colour larger than 1.4 mag. There are 14 such objects, and five of them are known EROs (their definition and selection criteria is given above in this section), which experience an intense mass-loss process (Gruendl et al. 2008). Table 8 lists all these objects with their names in order of the increasing values of the [6.4]−[9.3] colour. After that, the values of the [16.5]−[21.5] colour, T_d, λ_c, and F/Cont (30 μm) are given. All of these quantities are repeated from Table D.5. Finally, the values of the mass-loss rates with the corresponding reference are given. We note that there is only one object in the SMC at [6.4]−[9.3] = 1.36 mag, NGC 419 MIR 1, which also might be counted as an object with an intense mass-loss rate.

In the bottom panel of Fig. 15 we show the λ_c (30 μm) as a function of the [6.4]−[9.3] colour. The λ_c seems to be independent with the increasing [6.4]−[9.3] colour. As we discussed before, the large value of the λ_c for nine objects with the central wavelength above 29.7 μm may be result of the 30 μm feature weakness (see Table 7).

The [6.4]−[9.3] colour is only useful for the carbon-rich AGB objects, because the presence of the PAH features between 6 and 9 μm is interfering with that colour in the spectra of the post-AGB stars and PNe. The most offending is the PAH feature at 6.2 μm, therefore, we modified only the left side of the [6.4]−[9.3] colour so as to avoid this spectral feature. This gave us the new [5.8]−[9.3] colour, which was used for the post-AGB objects and PNe.

Table 8. List of AGB objects from the LMC, showing the intense mass-loss rates.

Name	[6.4]−[9.3] (mag)	[16.5]−[21.5] (mag)	T_d (K)	λ_c (30 μm) (μm)	F/Cont (30 μm)	Mass-loss rate ($M_\odot$ yr^{-1})	Mass-loss rate reference
IRAS 05053-6901	1.443 ± 0.013	0.407 ± 0.007	362 ± 5	28.778 ± 0.025	0.504 ± 0.009	...	...
IRAS 05125-7035	1.507 ± 0.013	0.354 ± 0.005	407 ± 5	28.586 ± 0.029	0.476 ± 0.006	...	...
IRAS 04535-6616	1.537 ± 0.016	0.399 ± 0.004	368 ± 3	28.411 ± 0.051	0.481 ± 0.005	...	...
IRAS 05416-6906	1.682 ± 0.017	0.472 ± 0.004	320 ± 2	28.738 ± 0.145	0.377 ± 0.009	...	...
IRAS 04518-6852	1.734 ± 0.020	0.434 ± 0.011	343 ± 7	28.885 ± 0.107	0.527 ± 0.015	...	...
IRAS 05568-6753	1.755 ± 0.016	0.570 ± 0.008	...	...	...	...	...
IRAS 05305-7251	2.127 ± 0.024	0.464 ± 0.006	324 ± 3	29.194 ± 0.262	0.398 ± 0.013	4.2×10^{-5}	(1)
IRAS 05315-7145	2.343 ± 0.031	0.784 ± 0.017	210 ± 4	29.956 ± 0.037	0.617 ± 0.020	1.7×10^{-4}	(1)
IRAS 05306-7032	2.349 ± 0.037	0.427 ± 0.032	347 ± 20	28.235 ± 0.136	0.338 ± 0.039	...	...
IRAS 04589-6825	2.356 ± 0.041	0.468 ± 0.026	321 ± 14	28.731 ± 0.186	0.481 ± 0.033	...	...
IRAS 05509-6956	2.483 ± 0.027	0.558 ± 0.008	278 ± 3	29.582 ± 0.084	0.300 ± 0.010	9.0×10^{-5}	(1)
IRAS 05026-6809	2.763 ± 0.031	0.625 ± 0.008	253 ± 3	30.477 ± 0.137	0.128 ± 0.009	...	...
IRAS 05495-7034	2.876 ± 0.041	1.066 ± 0.017	163 ± 2	30.322 ± 0.040	0.287 ± 0.020	2.3×10^{-4}	(1)
IRAS 05133-6937	3.024 ± 0.042	0.658 ± 0.007	242 ± 2	29.806 ± 0.221	0.167 ± 0.009	8.9×10^{-5}	(1)

Notes. The values of the T_d, λ_c, and F/Cont are taken from Table D.5.
References. (1) Gruendl et al. (2008).

While, the [6.4]−[9.3] colour for the AGB stars correlates well with mass-loss (Groenewegen et al. 2007), in case of the post-AGB objects and PNe the [5.8]−[9.3] one measures only optical depth of the detaching shell, and cannot be easily related to the mass-loss history. The geometrical effects (non-spherical symmetry, existence of discs and/or tori), do not allow for simple interpretation that decreasing optical depth is the manifestation of longer evolution after AGB and different mass-loss rates during this phase of evolution.

In Fig. 16 (four panels) we present the relations between the [5.8]−[9.3] and different colours used for determination of the T_d. Symbols on the graph are in line with Fig. 11. In the case of the post-AGB objects three different colours are used: [18.4]−[22.45] for group I (top panel), [18.4]−[22.75] for group II (second panel), and [17.95]−[23.2] for group III (third panel). In the bottom panel the PNe are shown with the [16.5]−[21.5] colour determined for them.

By comparing the positions of PNe in [5.8]−[9.3] colour with those for the post-AGB objects we see, that from statistical point of view the colours of PNe are bluer (their optical depths are smaller) than those for post-AGBs. The PNe colours concentrate between 2 and 3 mag with significant extension to the lower values of the [5.8]−[9.3] colour, while post-AGBs have colours larger than about 2.5 mag with significant contribution above 3 mag. The only exception being IRAS 00350-7436 with the [5.8]−[9.3] colour ∼1 mag on the top panel and IRAS 22223+4327 ([5.8]−[9.3] ∼1.9 mag) on the second panel. The values of the T_d are not known for them, because they belong to the objects with bad fits of continuum. However, their values of spectral indices are obtained. Finally we note that, while colours used for determination of the T_d are different for various objects shown in Fig. 16, there is a clear sign that PNe have statistically lower T_d (larger long-wavelength's colour) than post-AGBs, and AGBs shown in the third panel of Fig. 15.

4.2. Profiles of the 30 μm feature

The 30 μm feature appears in plenty of carbon-rich objects in many galaxies. As can be seen in Fig. 11, it is also visible in the wide range of the T_d. Apart the parameters of the feature, their profiles also might provide information about the differences of dust formation history in those galaxies. The profiles of the 30 μm feature were extracted from the continuum subtracted spectra. However, it was impossible to obtain the full profiles, because of the spectral coverage of the *Spitzer*. Nevertheless, they were long enough to contain the maxima of the emission and the subsequent declines. After the subtraction of the continuum, the profiles were normalised to the region around the maximum of the feature by dividing them by the average value of flux density calculated for this region. The range used for determination of the average value depended on the kind of object: 28.5–29.5 μm for the AGBs, and 28.5–30 μm for the post-AGBs. In the case of the PNe profiles we used the 30.5–32.5 μm normalisation range for low resolution spectra, and 30–31 μm for high resolution Galactic profiles. To determine those normalisation ranges, we also took into consideration the behaviour of the λ_c, and presence of nebular lines in a case of PNe. After normalisation, we determined 200 K intervals in the T_d up to 800 K, and one range for objects with the T_d > 800 K. All the objects were split in terms of the kind of object (AGB, post-AGB, and PN), hosted galaxy (SMC, LMC, Sgr dSph, and Milky Way), and given T_d range. The median profile was then calculated for each of such a sample, but on the assumption that there were at least three profiles. The spectra for the Galactic post-AGBs and PNe are composed of both resolutions. Because of this, we re-sampled the low resolution spectra to the high resolution wavelength grid using the linear interpolation before calculating the median profile.

Figure 17 shows the normalised median profiles of the 30 μm feature in the carbon-rich AGB stars for the four ranges of the T_d. The colours of lines on the graph are in line with the colours of the markers in Fig. 11. There is only one object in the LMC with the T_d below 200 K, thus we do not present any normalised median profile of the 30 μm feature in the AGB stars from this range. In addition, one Galactic object (IRAS 18120+4530) is excluded from median for T_d > 800 K. The λ_c for this object unusually exceeds 33 μm, therefore its normalised profile completely sticks out from the others (see Sect. 4.1 for details). All of AGB profiles of the 30 μm feature were derived from the low resolution *Spitzer* spectra. The normalised median profiles present a

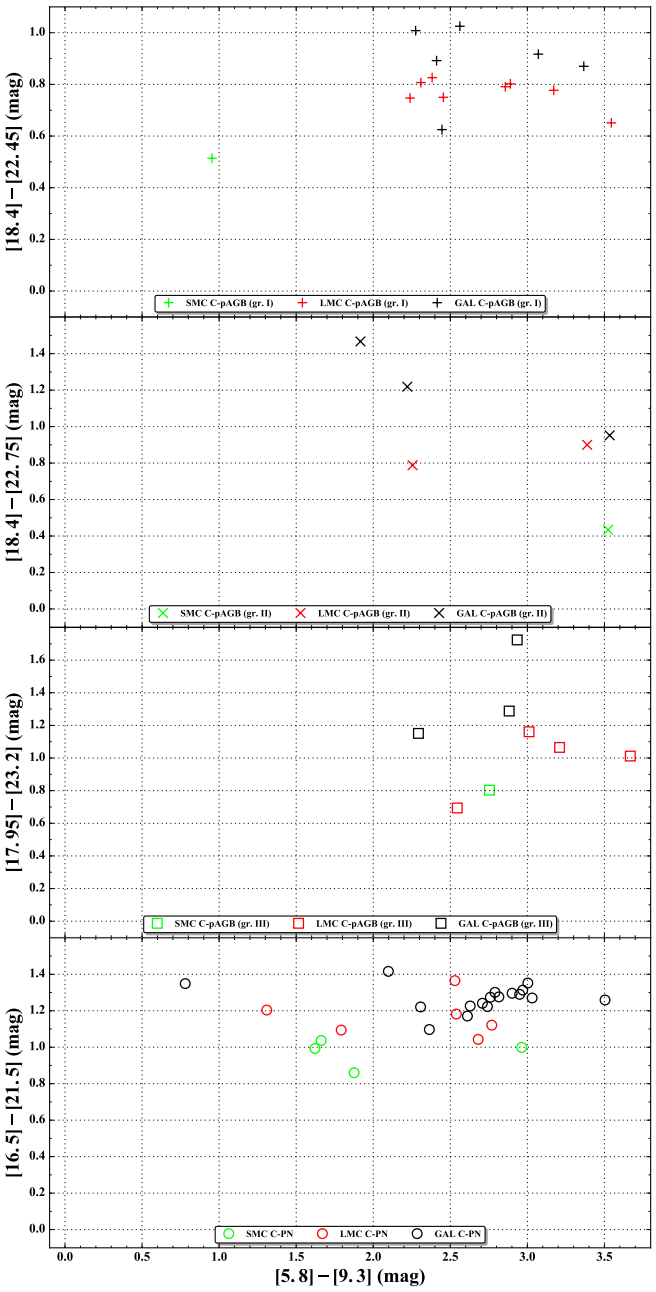

Fig. 16. Colours used for determination of the T_d in the different groups of the post-AGB objects. *From the top*: [18.4]−[22.45] (gr. I), [18.4]−[22.75] (gr. II), and [17.95]−[23.2] (gr. III) colour as a function of the [5.8]−[9.3] one. *Bottom panel*: [16.5]−[21.5] colour used for the determination of the T_d in PNe.

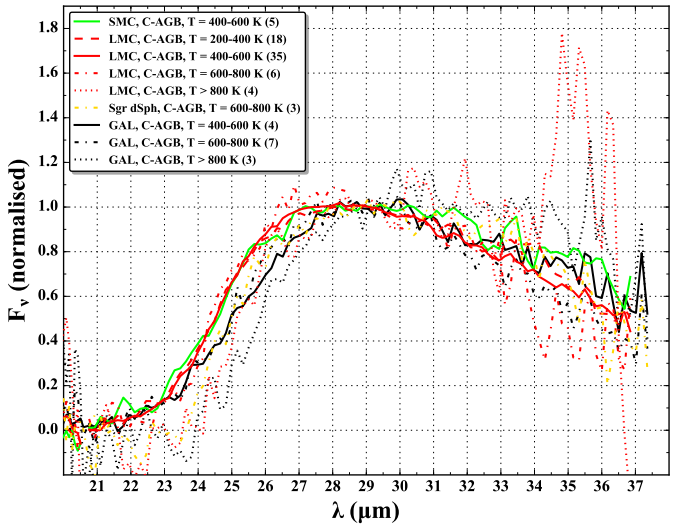

Fig. 17. Normalised median profiles of the 30 μm feature in the AGB stars calculated for the different ranges of the T_d. The brackets in the legend show the number of profiles taken to the calculation of a given median.

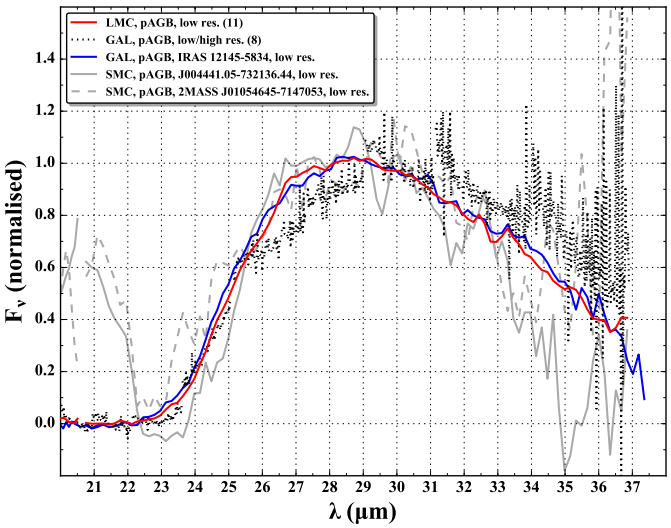

Fig. 18. Normalised median profiles of the 30 μm feature in the post-AGB stars. The brackets in the legend show the number of profiles taken to the calculation of a given median.

relatively steep rise from about 23 μm, and after reaching a maximum at around 29 μm, a gradual decline is visible up to the long wavelength *Spitzer* cut-off. The shape of particular median profiles of the 30 μm feature in the AGB stars looks uniformly for the different galaxies and the T_d ranges. Some changes in shape of the median profiles are noticeable for the T_d above 800 K. However, the 30 μm feature in those objects is relatively weak, and their profiles are noisy in general.

Figure 18 shows the normalised median profiles of the 30 μm feature in the carbon-rich post-AGB stars. All but two of the post-AGB stars in our sample lie in only one of the distinguished ranges of the T_d (below 200 K). Accordingly, we have not compared the median profiles as a function of the T_d. By the black dotted line we present the normalised median profile of the Galactic post-AGB objects. This median profile consists of high resolution spectra except one profile (shown by the blue solid line). There are only two post-AGB objects in the SMC with the derived normalised profiles of the 30 μm feature, therefore we show them for comparison instead of the median profile by the grey solid and dashed lines. The individual spectra for the SMC objects show the 21 μm feature, while the median spectra for the Milky Way and LMC make the contribution from the 21 μm emitters unseen. Our sample does not contain any of the post-AGB objects from the Sgr dSph galaxy.

The median profile for Galactic post-AGBs seems to be a little bit different than other low resolution spectra (median for the LMC and some individual spectra). Nevertheless, the high resolution median spectrum (Galactic) is quite noisy, so the difference may not be significant. In addition, the low and high resolution spectra from the CASSIS database were processed

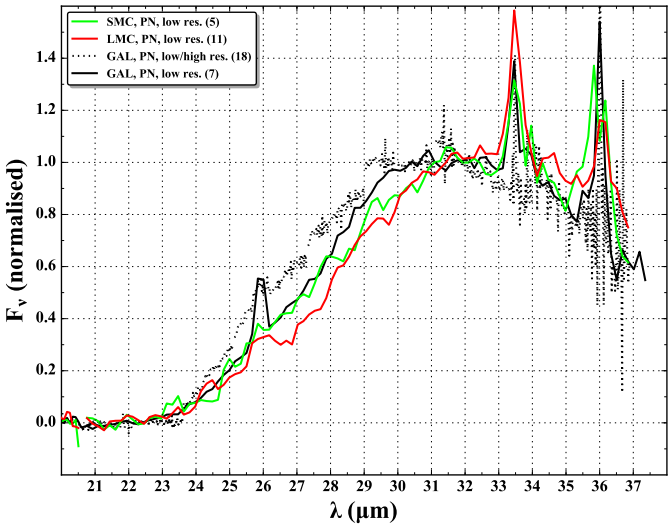

Fig. 19. Normalised median profiles of the 30 μm feature for the PNe. The brackets in the legend show the number of profiles taken to the calculation of a given median.

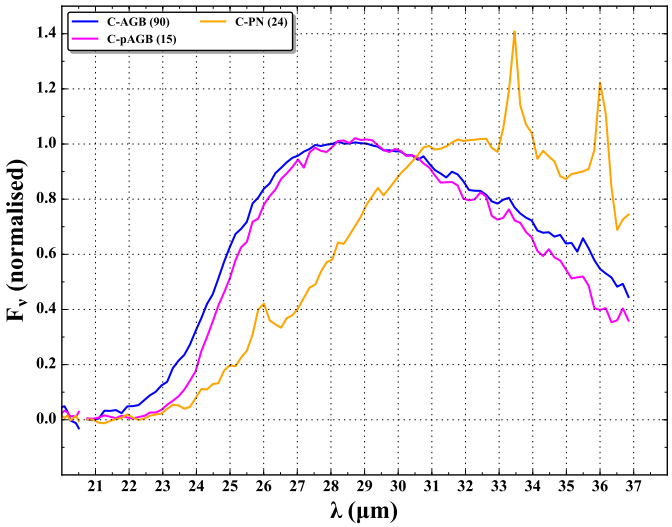

Fig. 20. Normalised median profiles (only low resolution) of the 30 μm feature for all the AGBs, post-AGBs, and PNe. The brackets in the legend show the number of profiles taken to the calculation of a given median.

using the different pipelines (see Lebouteiller et al. 2011, 2015), which might led to the distortion of profiles of the 30 μm feature.

The normalised median profiles of the 30 μm feature for the post-AGB objects look similar to the AGB ones in general. However, the blue edge of the individual normalised profiles might be affected by the presence of the strong 21 μm feature. The low resolution median profiles for the Milky Way and LMC objects show one common trace. The individual normalised profiles of the SMC post-AGB objects clearly confirm that shape.

Figure 19 illustrates the normalised median profiles of the 30 μm feature in the carbon-rich PNe. All the PNe lie in one of the distinguished ranges of the $T_{\rm d}$ (below 200 K) except one object. The colours of lines on the graph are in line with the colours of the markers in Fig. 11. The Sgr dSph galaxy contains only one PN with the 30 μm feature (Wray16-423), therefore the median profile is not shown. We also do not show the individual normalised profile for this object, because of the presence of the 16–24 μm feature (see Sect. 3.1). The comparison between the Galactic median profiles with low resolution spectra only, and median of all the Galactic ones (seven low and 11 high resolution) shows, that the difference in shape of the high resolution median profile is a matter of the various calibration of the spectra (different pipelines).

The most remarkable, the normalised median profiles of the PNe present clearly different shape than the profiles of the AGBs and post-AGBs (see also Fig. 20). The 30 μm emission appears around 24 μm with more gradual rise up to the maximum, which is significantly shifted towards the longer wavelengths in comparison with the AGB and post-AGB profiles. The shape of decline is more uncertain, because the profiles of the PNe are deformed by the presence of nebular lines – [O IV] at 25.89 μm, [S III] at 33.48 μm, and [Ne III] at around 36 μm are the most noticeable. The low resolution median profiles for the MCs and Galactic PNe show one common trace, with no significant difference between them. The individual median profiles from Figs. 17 to 19 together with every profile, which is a part of single median are presented in Appendix C.

The normalised median profiles of the 30 μm feature for the AGB stars look uniformly in the various ranges of the $T_{\rm d}$ and hosted galaxies. The low resolution median profiles for the post-AGB objects and PNe show the same behaviour. It allows us to collect the low resolution median profiles from all the analysed galaxies and create one common median profile of the 30 μm feature for the carbon-rich AGB stars, post-AGB objects, and PNe. However, the final medians include more normalised profiles than the previous ones, because this time we added profiles of objects, which previously were not included (less than three profiles, $T_{\rm d} < 200$ K for AGB stars or $T_{\rm d} > 200$ K for post-AGB objects). In case of AGB stars, five normalised profiles were added: one Sgr dSph, two SMC, one LMC, and one Galactic. In the case of post-AGB objects four profiles were added: two SMC, one LMC, and one Galactic, whereas in the case of PNe we added one LMC profile.

The comparison of the full median profiles is shown in Fig. 20. We distinguish the median profiles for the different phase of evolution by colour. The figure clearly shows the similarity of the median profiles for the AGB and post-AGB stars, but possibly the narrower 30 μm feature in the post-AGBs. The normalised median profile calculated for all PNe illustrates a distinctly different shape and a major shift towards the longer wavelength in comparison with the AGB and post-AGB ones, which is also noticeable in the obtained values of the $\lambda_{\rm c}$. The median profile for the PNe is also deformed by the presence of [O IV], [S III], and [Ne III] nebular lines. The second order polynomial fit to the regions of maxima of the 30 μm median profiles (between 26 and 32 μm for the AGB and post-AGB objects, and 27–35 μm for the PNe – but the [S III] line at 33.48 μm is removed from fit), shows the maximum (with the standard error around 0.02 μm) at 28.5 μm for the AGB, 29 μm for the post-AGB, and 32.5 μm for the PN profile. The shift of maximum between the normalised median profiles of the 30 μm feature in AGB and post-AGB stars is 0.5 μm whereas between AGBs and PNe is 3.6 μm.

4.3. Systematics of the method

The key issue in the analysis of the 30 μm feature is whether the shift in the $\lambda_{\rm c}$ is an indication of changes in the feature itself, or it is just an effect of the limited coverage of the *Spitzer* spectra. To investigate that, we analysed some ISO spectra from Hony et al. (2002). First, we made the continuum fits the way that the *Spitzer* data were fitted (24–36 μm), and then again with the full

wavelength coverage of the ISO spectra (24–45 μm). This allowed us to see what uncertainties are introduced by not having the continuum sampled on the longer side of the feature. This simple test showed that the values of the λ_c obtained with the full range of ISO spectra are always longer than those corresponding to the *Spitzer* range. The median of this difference is 3% in case of AGBs, 7% for post-AGBs, and 5% for PNe. It shows that, despite introducing a systematic shift to the shorter wavelength for the *Spitzer* range in all cases (AGBs, post-AGBs, and PNe), our method of continuum fit demonstrates that the shift of the λ_c in PNe is real and does not depend on the environment.

In Table 9 we list the medians of the λ_c for the AGB stars, post-AGB objects and PNe from Hony et al. (2002) and our work. The number of objects included into a given median is shown in the square bracket. The values in the last column of the Table are achieved by multiplying the medians from our work by the scaling factors discussed above. The scaled values of the λ_c are almost the same in case of AGB stars. On the other hand, for the post-AGB objects they are larger by 1.1 μm, while in the case of PNe they are smaller by the same value. These differences may be explained on the ground that we use different method of fitting the continuum. Hony et al. (2002) use the modified black-body continuum, while we use the black-body with a single temperature. The increase of the λ_c while going from 24 to 36 into 24–45 μm range concerns the Manchester method itself. The values of the λ_c are close to each other for AGB stars, because the continua of their spectra can be well defined by the black-body with a single temperature (with the dust emissivity index $p = 0$). When going into the post-AGB objects and PNe, the continua are not so well defined by a single black-body, and the non-zero value of dust emissivity index is often needed.

4.4. Summary

In this paper we present an analysis of the 30 μm dust feature as seen by *Spitzer*. Our sample consisted of 207 objects being in evolved stages of stellar evolution from four galaxies: five from the Sgr dSph (four carbon-rich AGB stars, one carbon-rich PN), 22 from the SMC (eight carbon-rich AGB stars, three carbon-rich post-AGB objects, and 11 PNe), 121 from the LMC (83 carbon-rich AGBs, 17 carbon-rich post-AGBs, and 21 carbon-rich PNe), and 59 from our Galaxy (17 carbon-rich AGBs, 23 carbon-rich post-AGBs, and 19 carbon-rich PNe). On the basis of this sample, we have created three online catalogues with photometric data and *Spitzer* IRS spectra for the objects with 30 μm feature from the SMC, LMC, and the Milky Way, separately. Five objects from the Sgr dSph were added to the Galactic catalogue with a special comment.

We applied the uniform method to fit the spectra with a black-body of a single temperature deduced from the Manchester method and its modifications. However, use of this method does not guarantee derivation of good continuum fits. We were unable to obtain the correct fits for 33 objects (16% of whole sample). In addition, 17 PNe and five post-AGB stars were also removed from the further analysis, because of the presence of the 16–24 μm feature in their *Spitzer* spectra. In case of two planetary nebulae (SMP LMC 51 and 79), and three post-AGB objects (IRAS 05370-7019, IRAS 05537-7015, and IRAS 21546+4721), the presence of the 16–24 μm feature has been recognised for the first time by us. The 16–24 μm feature affected the value of the [16.5]−[21.5] colour and precluded determination of correct continuum. Taking into account the above limitations we were able to obtain a good fit to the continuum for 152[14] objects (73%) from our initial sample. Then, subtraction of continuum allowed us to determine the parameters of the 30 μm feature, like its central wavelength, λ_c, and the strength, F/Cont. In addition, we determined the standard Manchester colour indices, like the [6.4]−[9.3] and [16.5]−[21.5], and some their modifications. One of them was done because of the new detections of the 16–18 μm feature in the spectra of nine PNe. We also found that the Galactic post-AGB object IRAS 11339-6004 has a 21 μm emission.

Table 9. Comparison of medians of the central wavelengths obtained for ISO and *Spitzer* spectra.

Source	λ_c (Hony et al. 2002) (μm)	λ_c (Our work) (μm)	$\lambda_c{}^{(a)}$ (Scaled) (μm)
AGBs	29.7 [36]	28.9 [91]	29.8
Post-AGBs	30.1 [14]	29.2 [35]	31.2
PNe	33.3 [13]	30.7 [23]	32.2

Notes. The square brackets contain the numbers of objects included into a given median. [(a)]Result of multiplying the third column by the scaling factor obtained from the ISO spectra (AGBs: 1.03, post-AGBs: 1.07, and PNe: 1.05).

Taking into account the Galactic sample of carbon stars with the ISO spectra (see Sloan et al. 2016), the strength of the 30 μm feature is the highest among Galactic objects. Moreover, this feature shows up at the highest dust temperature for the Galactic AGB stars. The first AGB objects with 30 μm feature in the LMC are visible below 900 K, whereas such objects in the SMC and Sgr dSph objects do not appear until T_d drops below 700 K. The strength of the feature increases until T_d drops to about 400 K, and then decreases to finally show again variety of values for post-AGB objects and PNe. The sample of the AGB stars is dominated by the LMC objects. The explanation of this behaviour lies in the fact, that it is much easier to create a carbon-rich star in the metal-poor environments (see e.g. Piovan et al. 2003). However, such a regularity is not visible in the SMC sample. The AGB objects with $T_d < 400$ K, seem to experience very large mass-loss rates, which may be responsible for the drop in the strength of the 30 μm feature due to self-absorption. During the post-AGB and PN phases, the strength of the 30 μm feature seems to not depend on the metallicity of galaxy.

Our analysis of central wavelength of the 30 μm feature shows that it is rather independent of T_d for AGB and post-AGB objects. The majority of the carbon-rich AGB and post-AGB objects occupy the region of the λ_c between about 28.5 and 29.5 μm. There are, however, some exceptions. These include: (a) AGB objects with $\lambda_c < 28$ μm, which is probably result of too high continuum derived, resulting in too low λ_c; (b) a group of ten AGB objects with 900 K > T_d > 300 K and $\lambda_c > 29.7$ μm, characterised by rather low F/Cont, which may cause uncertain determination of λ_c and its shift to the longer wavelengths; and (c) an interesting group of six AGB stars with low dust temperature and central wavelength larger than about 29.7 μm. In the last case, the low dust temperature suggests the large mass-loss rate, which is confirmed by estimation of mass-loss rates by Gruendl et al. (2008). In this sense, cold AGB dust may have

[14] This number includes three objects for which only T_d is given in Table D.5: MSX LMC 782, MSX LMC 787 showing the problem with calibration (see Sect. 3.2 for details), and MSX LMC 974 with very noisy spectrum over 32 μm.

central wavelength of the 30 μm feature shifted towards longer values. On the other hand even colder dust in post-AGB objects has a λ_c similar to that of most AGB stars.

From our analysis, we see that the central wavelengths shift towards longer values, typically from 29.5 and 31.5 μm, in case of PNe. Hony et al. (2002) suggested that such shift is caused by the low temperature of the feature carrier, or change in shape of dust particles. However, we see several post-AGB objects with similar dust temperature, but much lower central wavelength than in PNe. Therefore, we expect that dust processing (e.g. due to irradiation by UV photons from central stars of PNe) may be more important in shifting central wavelength of the 30 μm feature towards larger values. Finally, we note that it seems the Galactic PNe have rather smaller λ_c values than their MCs counterparts. If our suggestions are correct, this could mean that processing of the 30 μm feature carrier is more efficient in the MCs than in the Milky Way.

We have also searched for the median profiles of the 30 μm feature in different galaxies and/or dust temperature. Before determination of such profiles spectra were normalised to the average flux in the ranges typical for each class of objects and/or resolution of the spectra. The average fluxes were determined in range 28.5–29.5 μm in case of AGB stars, 28.5–30 μm in case of post-AGB objects, 30.5–32.5 μm for low resolution spectra of PNe, and 30–31 μm for high resolution spectra of PNe. We have shown that the averaged shapes of the 30 μm feature do not change as a function of metallicity for investigated objects. However, the shape of the feature in PNe is clearly different (not only the central wavelength) than shape of the feature in AGB or post-AGB objects.

Acknowledgements. This work was financially supported by the National Science Center (NCN) of Poland through grant No. 2014/15/N/ST9/04629. R.S. acknowledges support from the NCN grant No. 2016/21/B/ST9/01626. We have made extensive use of the SIMBAD and Vizier databases operated at the Centre de Données Astronomiques de Strasbourg. We also collected low and high resolution spectra from the Combined Atlas of Sources with *Spitzer* IRS spectra (CASSIS), which is a product of the IRS instrument team, supported by NASA and JPL.

References

Benjamin, R. A., Churchwell, E., Babler, B. L., et al. 2003, PASP, 115, 953
Bernard-Salas, J., Peeters, E., Sloan, G. C., et al. 2009, ApJ, 699, 1541
Bernard-Salas, J., Cami, J., Peeters, E., et al. 2012, ApJ, 757, 41
Boersma, C., Bauschlicher, C. W., Allamandola, L. J., et al. 2010, A&A, 511, A32
Cami, J., Bernard-Salas, J., Peeters, E., & Malek, S. E. 2010, Science, 329, 1180
Cerrigone, L., Hora, J. L., Umana, G., et al. 2011, ApJ, 738, 121
Churchwell, E., Babler, B. L., Meade, M. R., et al. 2009, PASP, 121, 213
Cutri, R. M., Skrutskie, M. F., & van Dyk, S. 2006, Vizier On-line Data Catalog: II/281
Duley, W. W. 2000, ApJ, 528, 841
Egan, M. P., Price, S. D., & Kraemer, K. E. 2003, BAAS, 35, 1301
Fitzpatrick, E. L. 1991, PASP, 103, 1123
Forrest, W. J., Houck, J. R., & McCarthy, J. F. 1981, ApJ, 248, 195
Frankowski, A. 2003, A&A, 406, 265
García-Hernández, D. A., Manchado, A., García-Lario, P., et al. 2010, ApJ, 724, L39
García-Hernández, D. A., Villaver, E., García-Lario, P., et al. 2012, ApJ, 760, 107
Goebel, J. H., & Moseley, S. H. 1985, ApJ, 290, L35
Gordon, K. D., Meixner, M., Meade, M. R., et al. 2011, AJ, 142, 102
Grishko, V. I., Tereszchuk, K., Duley, W. W., & Bernath, P. 2001, ApJ, 558, L129
Groenewegen, M. A. T., van den Hoek, L. B., & de Jong, T. 1995, A&A, 293, 381
Groenewegen, M. A. T., Wood, P. R., Sloan, G. C., et al. 2007, MNRAS, 376, 313
Groenewegen, M. A. T., Sloan, G. C., Soszyński, I., & Petersen, E. A. 2009, A&A, 506, 1277
Gruendl, R. A., Chu, Y.-H., Seale, J. P., et al. 2008, ApJ, 688, L9
Helou, G., & Walker, D. W., eds. 1988, Infrared Astronomical Satellite (IRAS) Catalogs and Atlases. 7, 1
Herwig, F. 2005, ARA&A, 43, 435
Hony, S., Waters, L. B. F. M., & Tielens, A. G. G. M. 2002, A&A, 390, 533
Hrivnak, B. J., Volk, K., & Kwok, S. 2009, ApJ, 694, 1147
Hrivnak, B. J., Lu, W., Maupin, R. E., & Spitzbart, B. D. 2010, ApJ, 709, 1042
Hrivnak, B. J., Lu, W., Volk, K., et al. 2015, ApJ, 805, 78
Ishihara, D., Onaka, T., Kataza, H., et al. 2010, A&A, 514, A1
Kamath, D., Wood, P. R., Soszyński, I., & Lebzelter, T. 2010, MNRAS, 408, 522
Kwok, S., & Zhang, Y. 2013, ApJ, 771, 5
Kwok, S., Volk, K. M., & Hrivnak, B. J. 1989, ApJ, 345, L51
Lagadec, E., Zijlstra, A. A., Sloan, G. C., et al. 2009, MNRAS, 396, 598
Lagadec, E., Zijlstra, A. A., Mauron, N., et al. 2010, MNRAS, 403, 1331
Lagadec, E., Sloan, G. C., Zijlstra, A. A., Mauron, N., & Houck, J. R. 2012, MNRAS, 427, 2588
Lasker, B. M., Lattanzi, M. G., McLean, B. J., et al. 2008, AJ, 136, 735
Lebouteiller, V., Bernard-Salas, J., Sloan, G. C., & Barry, D. J. 2010, PASP, 122, 231
Lebouteiller, V., Barry, D. J., Spoon, H. W. W., et al. 2011, ApJS, 196, 8
Lebouteiller, V., Barry, D. J., Goes, C., et al. 2015, ApJS, 218, 21
Lombaert, R., de Vries, B. L., de Koter, A., et al. 2012, A&A, 544, L18
Matsuura, M., Bernard-Salas, J., Lloyd Evans, T., et al. 2014, MNRAS, 439, 1472
Mauron, N., Gigoyan, K. S., Berlioz-Arthaud, P., & Klotz, A. 2014, A&A, 562, A24
Meixner, M., Gordon, K. D., Indebetouw, R., et al. 2006, AJ, 132, 2268
Messenger, S. J., Speck, A., & Volk, K. 2013, ApJ, 764, 142
Moshir, M. 1990, in IRAS Faint Source Catalogue, Version 2.0 1990
Neugent, K. F., Massey, P., Skiff, B., & Meynet, G. 2012, ApJ, 749, 177
Otsuka, M. 2015, MNRAS, 452, 4070
Otsuka, M., Kemper, F., Hyung, S., et al. 2013, ApJ, 764, 77
Otsuka, M., Kemper, F., Cami, J., Peeters, E., & Bernard-Salas, J. 2014, MNRAS, 437, 2577
Peeters, E., Mattioda, A. L., Hudgins, D. M., & Allamandola, L. J. 2004, ApJ, 617, L65
Perea-Calderón, J. V., García-Hernández, D. A., García-Lario, P., Szczerba, R., & Bobrowsky, M. 2009, A&A, 495, L5
Piovan, L., Tantalo, R., & Chiosi, C. 2003, A&A, 408, 559
Raman, V. V., Anandarao, B. G., Janardhan, P., & Pandey, R. 2017, MNRAS, 470, 1593
Samus', N. N., Kazarovets, E. V., Durlevich, O. V., Kireeva, N. N., & Pastukhova, E. N. 2017, Astron. Rep., 61, 80
Skrutskie, M. F., Cutri, R. M., Stiening, R., et al. 2006, AJ, 131, 1163
Sloan, G. C., Kraemer, K. E., Matsuura, M., et al. 2006, ApJ, 645, 1118
Sloan, G. C., Matsunaga, N., Matsuura, M., et al. 2010, ApJ, 719, 1274
Sloan, G. C., Matsuura, M., Lagadec, E., et al. 2012, ApJ, 752, 140
Sloan, G. C., Lagadec, E., Zijlstra, A. A., et al. 2014, ApJ, 791, 28
Sloan, G. C., Kraemer, K. E., McDonald, I., et al. 2016, ApJ, 826, 44
Smolders, K., Neyskens, P., Blommaert, J. A. D. L., et al. 2012, A&A, 540, A72
Soszyński, I., Udalski, A., Szymański, M. K., et al. 2009, Acta Astron., 59, 239
Soszyński, I., Udalski, A., Szymański, M. K., et al. 2011, Acta Astron., 61, 217
Speck, A. K., Corman, A. B., Wakeman, K., Wheeler, C. H., & Thompson, G. 2009, ApJ, 691, 1202
Stanghellini, L., García-Lario, P., García-Hernández, D. A., et al. 2007, ApJ, 671, 1669
Stanghellini, L., García-Hernández, D. A., García-Lario, P., et al. 2012, ApJ, 753, 172
Szczerba, R., Omont, A., Volk, K., Cox, P., & Kwok, S. 1997, A&A, 317, 859
Szczerba, R., Siódmiak, N., Stasińska, G., & Borkowski, J. 2007, A&A, 469, 799
Szczerba, R., Siódmiak, N., Stasińska, G., et al. 2012, IAU Symp., 283, 506
The Denis Consortium 2005, The DENIS database, 3rd Release
Villaver, E., Stanghellini, L., & Shaw, R. A. 2003, ApJ, 597, 298
Volk, K., Hrivnak, B. J., Matsuura, M., et al. 2011, ApJ, 735, 127
Whitelock, P. A., Feast, M. W., Menzies, J. W., & Catchpole, R. M. 1989, MNRAS, 238, 769
Whitelock, P. A., Feast, M. W., van Loon, J. T., & Zijlstra, A. A. 2003, MNRAS, 342, 86
Woods, P. M., Oliveira, J. M., Kemper, F., et al. 2011, MNRAS, 411, 1597
Wright, E. L., Eisenhardt, P. R. M., Mainzer, A. K., et al. 2010, AJ, 140, 1868
Yamamura, I., Makiuti, S., Ikeda, N., et al. 2010, VizieR Online Data Catalog: II/298
Zaritsky, D., Harris, J., Thompson, I. B., Grebel, E. K., & Massey, P. 2002, AJ, 123, 855
Zaritsky, D., Harris, J., Thompson, I. B., & Grebel, E. K. 2004, AJ, 128, 1606
Zhang, Y., & Kwok, S. 2011, ApJ, 730, 126
Zhang, K., Jiang, B. W., & Li, A. 2009, ApJ, 702, 680
Zhang, Y., Kwok, S., & Hrivnak, B. J. 2010, ApJ, 725, 990
Zijlstra, A. A., Matsuura, M., Wood, P. R., et al. 2006, MNRAS, 370, 1961

Appendix A: Full sample

In the case of post-AGB objects and PNe from Sloan et al. (2014), we added one PN (SMP SMC 17) to the list of the SMC objects, along with adding one post-AGB object (SAGE J051825-700532), and 11 PNe (SMP LMC 19, SMP LMC 27, SMP LMC 34, SMP LMC 36, SMP LMC 38, SMP LMC 52, SMP LMC 61, SMP LMC 71, SMP LMC 75, SMP LMC 78, and SMP LMC 79) to the list of the LMC objects. On the other hand, we deleted four objects from the LMC (SMP LMC 11 and 25; IRAS 05315-7145 and IRAS 05495-7034 were removed from the post-AGB list, because we classified them as AGB stars). We present our arguments for these changes below.

SMP SMC 17 is classified by Stanghellini et al. (2007) as an intermediate-excitation PN ([Ar III], [S IV], and [Ne III] nebular lines are visible) showing the PAH features at 6.2, 7.7, and 8.6 μm, which are blended with a broader 8 μm plateau feature, and 11.3 μm at the top of a broader 12 μm plateau feature (see e.g. Kwok & Zhang 2013). The *Spitzer* spectrum also shows a feature around 19 μm, which could be attributed to the fullerenes (C_{60}), but its identification seems to be doubtful (García-Hernández et al. 2012). We also find the 16–18 μm feature in the spectrum of this object (see Sect. 3.1 for details).

SAGE J051825-700532 is classified by Matsuura et al. (2014) as a carbon-rich AGB star. The *Spitzer* spectrum shows only weak SiC emission, with no sign of the PAH bands, and an easily visible 30 μm feature. We find an optical counterpart 0″.89 away (using IRAC[15] coordinates as the reference position), and if it is a good match the SED suggests that we are dealing with a post-AGB object having a detached dust shell. We also find a matching entry in the OGLE-III catalogue of long-period variables in the LMC (Soszyński et al. 2009). This object is identified as an "OGLE small amplitude red giant" with two pulsation periods of 16.8 and 15.9 days (*I*-band) and the corresponding amplitudes of 0.006 and 0.008 mag. These pulsation periods are too short for an AGB star, but would be consistent with variability during the post-AGB phase. Taking all these arguments into account, we classify SAGE J051825-700532 as a carbon-rich post-AGB object.

For the additional LMC PNe, five were taken from Stanghellini et al. (2007). SMP LMC 19 is classified by them as a carbon-rich PN. The *Spitzer* spectrum shows PAHs, especially the 11.3 μm band which is clearly visible on top of the 12 μm plateau, and nebular lines such as [Ar III], [S III], [S IV], [Ne II], [Ne III], [Ne V], and a very strong [O IV] line. The 16–18 μm feature and the broad 16–24 feature are visible as well (see Sect. 3.1 for details). This set of lines indicates an object with high excitation PN (Stanghellini et al. 2007). The *Spitzer* spectrum of SMP LMC 27 is classified by Stanghellini et al. (2007) as a featureless intermediate-excitation PN, which means that there is a lack of visible dust features, except for a clear 30 μm feature. The *Spitzer* spectrum shows [S III], [S IV], and [Ne III] nebular lines. SMP LMC 34 is also classified by Stanghellini et al. (2007) as a featureless and intermediate-excitation PN spectrum like SMP LMC 27. The 30 μm feature is again the only indicator of the carbon-rich nature of this object. The most obvious nebular lines in the *Spitzer* spectrum are: [S III], [S IV], [Ne II], and [Ne III]. The *Spitzer* spectrum of SMP LMC 71 shows clearly visible carbon-rich dust features: PAHs, together with the 8, 12 μm plateau features, and the 16–18 μm feature. The [Ar III], [S III], [S IV], [Ne V], [Ne III], and [O IV] nebular lines are visible in the spectrum, which imply a very high excitation by a star with $T_{\rm eff} \sim 80\,000$ K, and $\log L/L_{\odot} < 4.27$ (Villaver et al. 2003). The *Spitzer* spectrum of SMP LMC 79 is dominated by PAH bands, together with the 8 and 12 μm plateau features, and the 16–18 μm feature. Another interesting dust emission feature seen in the spectrum is a broad 16–24 μm feature. The nebular lines visible in the spectrum are [S III], [S IV], [Ne III], and [O IV], which are characteristic for high excitation PN (Stanghellini et al. 2007).

Another four LMC PNe were taken from Bernard-Salas et al. (2009). According to the authors, all of them are the carbon-rich sources. The *Spitzer* spectrum of the first object, SMP LMC 36, shows very strong PAH features as in the spectrum of SMP LMC 79, including the 8 and 12 μm plateau features, and the 16–18 μm feature, but with a lack of the broad 16–24 μm feature. The nebular lines visible in the spectrum are [Ar III], [S III], [S IV], [Ne III], [Ne V], and [O IV], which indicate a high excitation PN. SMP LMC 38 has a [WR] central star and its spectrum shows strong PAHs with the 8 and 12 μm plateau features, and the 16–18 μm feature. The nebular [S III], [S IV], and [Ne III] lines are visible in the spectrum; thus we are dealing with an intermediate-excitation PN. SMP LMC 61 has also a [WR] central star and its spectrum shows strong PAHs with the 8 and 12 μm plateau features, the 16–18 μm feature, and nebular lines typical for intermediate-excitation PN: [Ar III], [S III], [S IV], [Ne II], and [Ne III]. The next object in this group is SMP LMC 78. The *Spitzer* spectrum shows the easily visible PAHs with the 8 and 12 μm plateau features, the 16–18 μm feature, the broad 16–24 feature, and nebular lines typical for a high excitation PN: [Ar III], [S III], [S IV], [Ne II], [Ne III], [Ne V], and [O IV].

The last two PNe that we have added have been analysed by Matsuura et al. (2014). The spectrum of SMP LMC 52 does not show any sign of PAHs. However, it has a very clearly visible 30 μm feature, which is the only indicator of carbon-rich nature of this object. The presence of the nebular lines of [Ar III], [S III], [S IV], [Ne III], [Ne V], and [O IV] indicates that this object is a high excitation PN. The spectrum of SMP LMC 75 contains strong PAHs, the 8 and 12 μm plateau features, and the 16–18 μm feature. In the spectrum the nebular [S III], [S IV], [Ne II] and [Ne III] lines are visible, which corresponds to this being an intermediate-excitation PN.

We rejected two objects from the Sloan et al. (2014) LMC sample. SMP LMC 11 is a member of their "red group" for which the only requirement is a red continuum. It shows weak PAH features, but we conclude that the spectrum does not contain the 30 μm feature. SMP SMC 25 is also a member of the red group, but we rejected this object, because crystalline silicates are visible.

In addition, the Sloan et al. (2014) sample contains two objects from the LMC with the 30 μm feature, but which do not have a well defined classification: IRAS 05315-7145 and IRAS 05495-7034. Both of them are assigned to the red group in their paper. Here, we classify them from the literature. The first object, IRAS 05315-7145, is classified by Gruendl et al. (2008) as an ERO. The bolometric luminosity of our target is 9500 $L_{\odot}$, whereas the estimated mass-loss rate is $1.7 \times 10^{-4}\,M_{\odot}\,{\rm yr}^{-1}$. Woods et al. (2011) classify it as a carbon-rich AGB star. However, we do not find any information about the long period variability, which is characteristic of AGB stars. The *Spitzer* spectrum shows the 30 μm feature, but the SiC is not well visible and there is a lack of C_2H_2 absorption. On the basis of the collected information, we assume this is a carbon-rich AGB star. The second object, IRAS 05495-7034 is assigned by

[15] IRAC: Infrared Array Camera on board *Spitzer*.

Gruendl et al. (2008) to the ERO group, with a bolometric luminosity 11 100 $L_{\odot}$ and an estimated mass-loss rate of $2.3 \times 10^{-4}\,M_{\odot}\,\mathrm{yr}^{-1}$. Woods et al. (2011) mark this object as a carbon-rich AGB star. The SED of the source in our catalogue (see Sect. 2.2) is typical of an AGB star. Because of the classification of IRAS 05315-7145 and IRAS 05495-7034 as carbon-rich AGB stars, these objects have been moved from the post-AGB sample of Sloan et al. (2014), and treated as the additions to the carbon-rich AGB sample of Sloan et al. (2016).

We re-examined the sample from Sloan et al. (2016), which consists of 184 carbon-rich AGB stars from the MCs, and we selected 89 objects showing the 30 μm feature. Our sample contains almost all the objects for which Sloan et al. (2016) reported the values of the strength of the 30 μm feature (see Sect. 3.2 for the definition of this parameter). However, after re-analysing the spectra, we excluded MSX LMC 036 and OGLE J051306.52-690946.4 because we did not detect the 30 μm feature (see Sect. 3.2 for details). Moreover, our sample contains two objects (IRAS 05026-6809 and MSX LMC 494) for which the values of the strength of the feature were previously not determined. However, we consider them as true 30 μm sources, because the features are measurable, and the end of the *Spitzer* spectrum is turning down.

We found four carbon-rich AGB stars in the Sgr dSph galaxy, which were analysed by Lagadec et al. (2009): Sgr 3 (IRAS F18413-3040), Sgr 7 (IRAS F18436-2849), Sgr 15 (IRAS F18555-3001), and Sgr 18 (IRAS 19013-3117). All of them are long-period pulsators with periods between 417 and 485 days. Their *Spitzer* spectra show typical carbon-rich dust feature of SiC, and molecular absorptions of C_2H_2 at 7.5 and 13.7 μm. We found only one PN in this galaxy with a *Spitzer* spectrum, Wray16-423, which was analysed in detail by Otsuka (2015). This spectrum shows the weak 8 and 12 μm plateau features as well as the broad 16–24 μm feature.

The Galactic sample analysed here consists of 59 objects (carbon-rich AGBs, post-AGBs, and PNe). The part of our sample containing the carbon-rich AGB objects is different from the work by Sloan et al. (2016), because their list is based on ISO spectra. We found ten S-type stars, which are in the transition phase between M-type and C-type AGB stars (Smolders et al. 2012): CSS 987, GY Lac, CSS 1, CSS 466, CSS 657, CSS 380, CSS 661, CSS 749, CSS 438, and AO Gem. Lagadec et al. (2012) analysed seven objects towards the Galactic halo: IRAS 04188+0122, IRAS 08427+0338, Lyngå 7 V1, IRAS 16339-0317, IRAS 18120+4530, IRAS 18384-3310, and IRAS 19074-3233. These objects' membership of the Galactic halo or the Galactic thick disc is established by Lagadec et al. (2010, 2012). According to the authors, IRAS 04188, IRAS 08427, and Lyngå 7 V1 are members of the Galactic thick disc population, whereas IRAS 16339, IRAS 18120, IRAS 18384, and IRAS 19074 belong to the Galactic halo. In addition, IRAS 18384 and IRAS 19074 are included to the analysis of carbon-rich AGB stars in the Sgr dSph galaxy (Lagadec et al. 2009), but their radial velocity study of the optical spectra shows that they clearly belong to the Milky Way (i.e. they are in the foreground). Furthermore, the *Spitzer* spectrum of Lyngå 7 V1 is first published by Sloan et al. (2010) after their observations of Galactic globular clusters. It is not clear whether this object is a true member of the globular cluster or not.

The most numerous sources in the Milky Way sample are carbon-rich post-AGB objects. Seven of them were analysed by Hrivnak et al. (2009): IRAS 05113+1347, IRAS 05341+0852, IRAS 06530-0213, IRAS 07430+1115, IRAS 19477+2401, IRAS 22574+6609, and IRAS 23304+6147. All of them have high resolution spectra, and they possess the 21 μm and 30 μm features. The short-high part of the *Spitzer* spectrum of IRAS 19477 is unusable (probably due to a bad positioning; see Hrivnak et al. 2009 for details). IRAS 23304 has been previously observed by the ISO mission, and it is included in the original paper reporting the discovery of the 21 μm feature (Kwok et al. 1989). The discovery list contains one more object in the current sample – IRAS 04296+3429. The *Spitzer* spectrum of this source was investigated by Zhang et al. (2010), as well as the spectra of the carbon-rich post-AGB objects IRAS 22223+4327 and IRAS 01005+7910. In the case of IRAS 01005 the 21 μm feature is not visible, though the broad 16–24 μm feature appears in the spectrum, reported by Zhang et al. (2010). This object is also the first example of a carbon-rich post-AGB source in which fullerene C_{60} was found (Zhang & Kwok 2011). Another three carbon-rich post-AGB objects were analysed by Cerrigone et al. (2011) and show the 21 μm feature: IRAS 13245-5036, IRAS 14429-4539, and IRAS 15482-5741. In the low-resolution *Spitzer* spectrum of IRAS 13245, a big shift between the SL and LL segments is visible. Seven additional carbon-rich post-AGB objects were included after inspection of the *Spitzer* spectra from *Spitzer* General Observer program 30258 (PI: P. Garcia-Lario). They are: IRAS 11339-6004, IRAS 15038-5533, IRAS 15229-5433, IRAS 15531-5704, IRAS 16296-4507, IRAS 18533+0523, and IRAS 21525+5643. There are two 21 μm sources among this group: IRAS 11339, which is a new detection in our work, and IRAS 18533. The inspection of the *Spitzer* spectra from program 50116 (PI: G. Fazio) provided us with another three carbon-rich post-AGB objects: IRAS 12145-5834, IRAS 14325-4628, and IRAS 21546+4721. One object in this group, IRAS 21546, shows the emission of fullerene (Raman et al. 2017).

The list of carbon-rich Galactic PNe is based on 15 objects observed by Stanghellini et al. (2012): PN K3-19, PN K3-31, PN M1-71, PN K3-37, PN K3-39, PN K3-54, PN K3-62, PN M1-5, PN M1-12, PN PB 2, Hen 2-5, Hen 2-26, Hen 2-41, Hen 2-68, and Hen 2-115. Four objects in this group show fullerene emission: PN K3-54, PN K3-62, PN M1-12, and Hen 2-68. In addition, Otsuka et al. (2013) report the presence of the 16–24 μm feature in the spectrum of PN M1-12. The presence of this feature in the spectrum that we have analysed is not obvious, thus we have not removed it from further analysis (see Sect. 3.1). The sample of PNe is supplemented by two carbon-rich objects from Perea-Calderón et al. (2009), who observed PNe in the Galactic bulge: PN M1-20 and PN Tc 1. The planetary nebula Tc 1 is the best example of a fullerene source (Cami et al. 2010). The spectrum of PN M1-20 also shows fullerene emission. In addition the list of the fullerene-containing PNe includes the carbon-rich object PN M1-11, studied in detail by Otsuka et al. (2013). The authors also report the presence of the broad 16–24 μm feature in this object. The last carbon-rich PN in the Galactic sample is PN K3-60, which was included after inspection of data from the program 30430 (PI: H. Dinerstein).

Appendix B: Whole spectra

Figures B.1–B.11 show the *Spitzer* spectra, which have been analysed in this work.

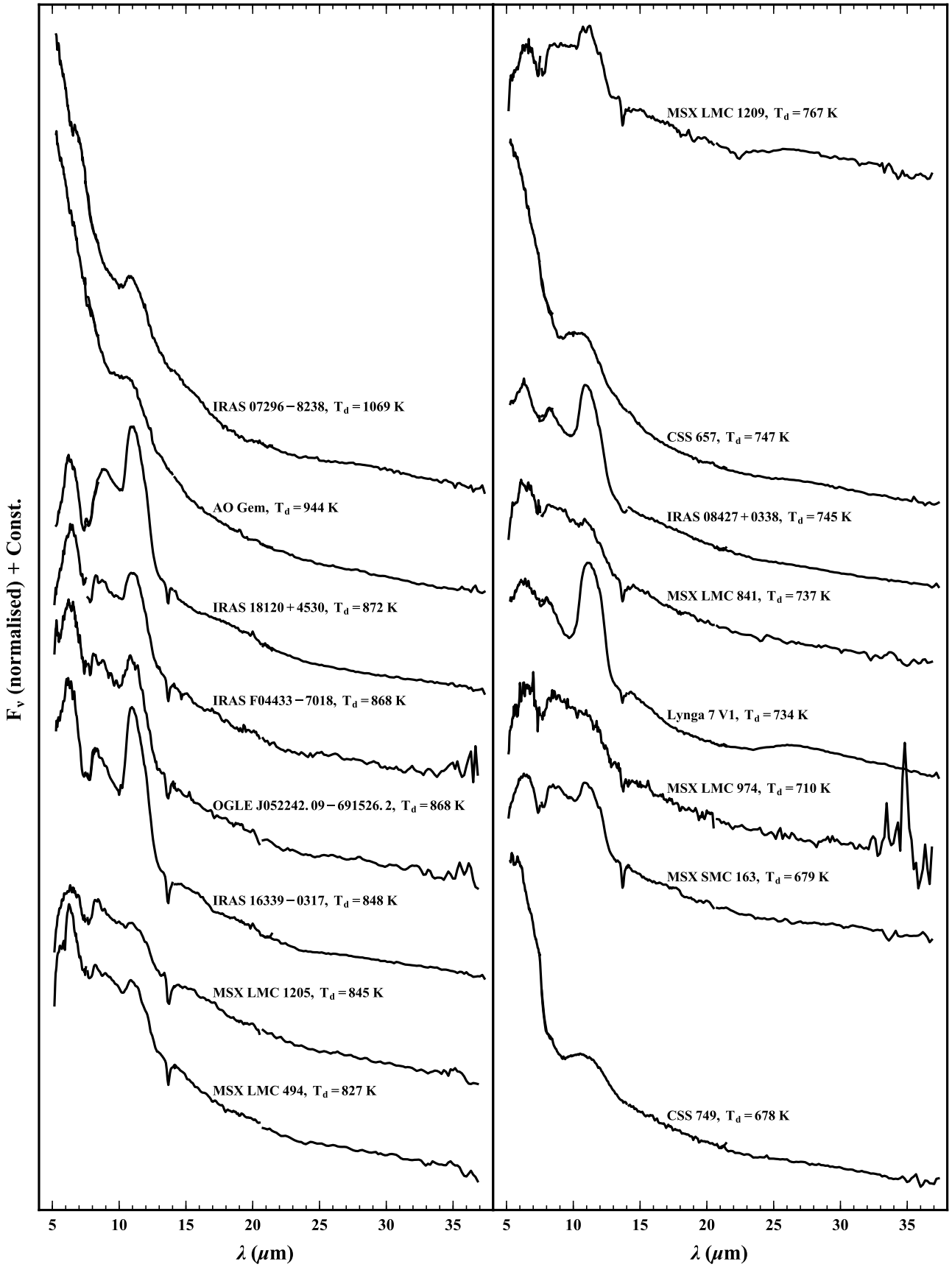

Fig. B.1. Overview of the *Spitzer* spectra (black solid lines) of the carbon-rich AGB stars with the 30 μm feature. The spectra are ordered according to the $T_{\rm d}$ from high to low temperature, top to bottom, and left to right, and are normalised to the flux density at 18 μm and offset for clarity. The names of objects and values of the $T_{\rm d}$ are shown above the spectra.

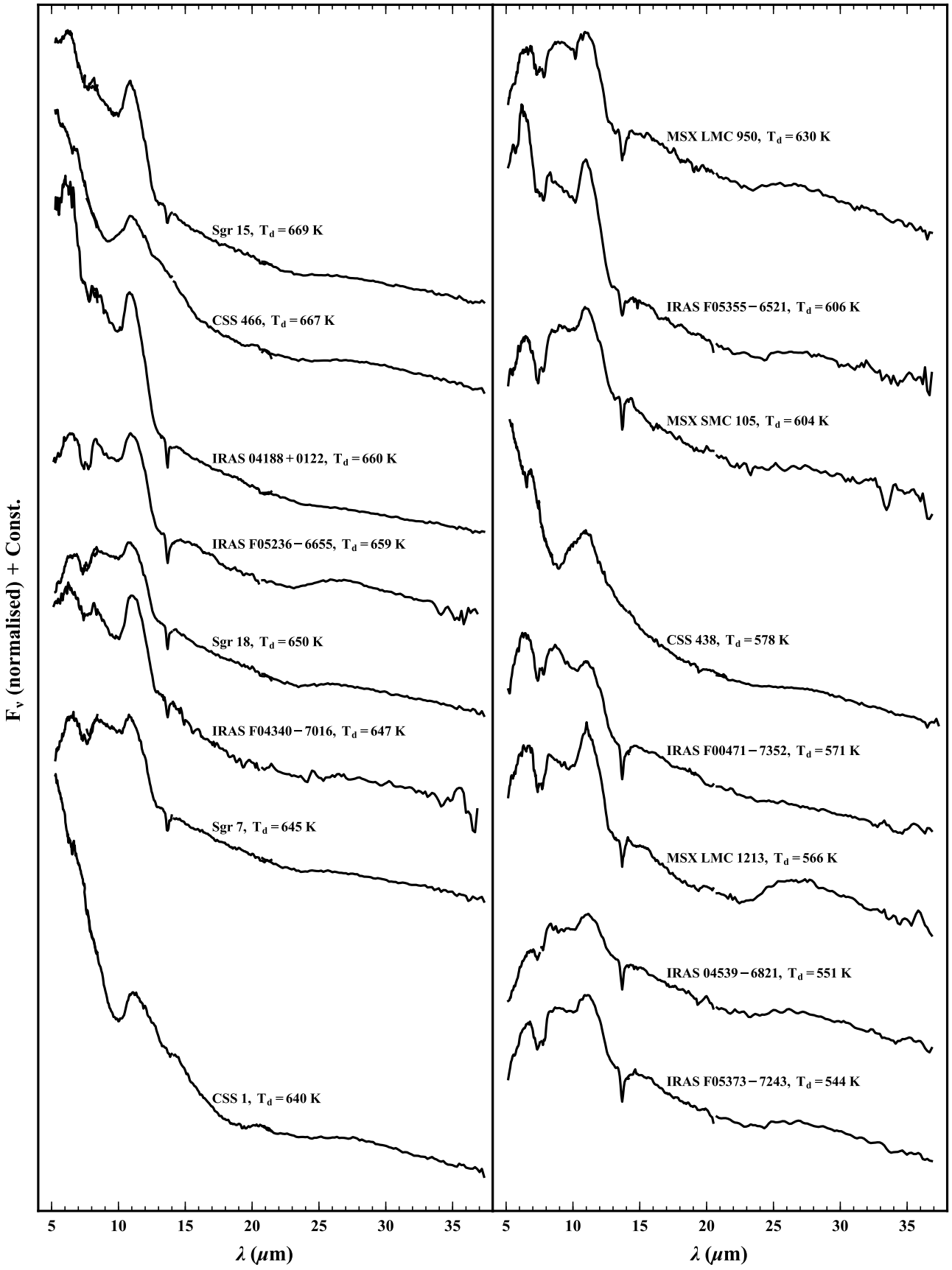

Fig. B.2. Overview of the *Spitzer* spectra (black solid lines) of the carbon-rich AGB stars with the 30 μm feature. The spectra are ordered according to the T_d from high to low temperature, top to bottom, and left to right, and are normalised to the flux density at 18 μm and offset for clarity. The names of objects and values of the T_d are shown above the spectra.

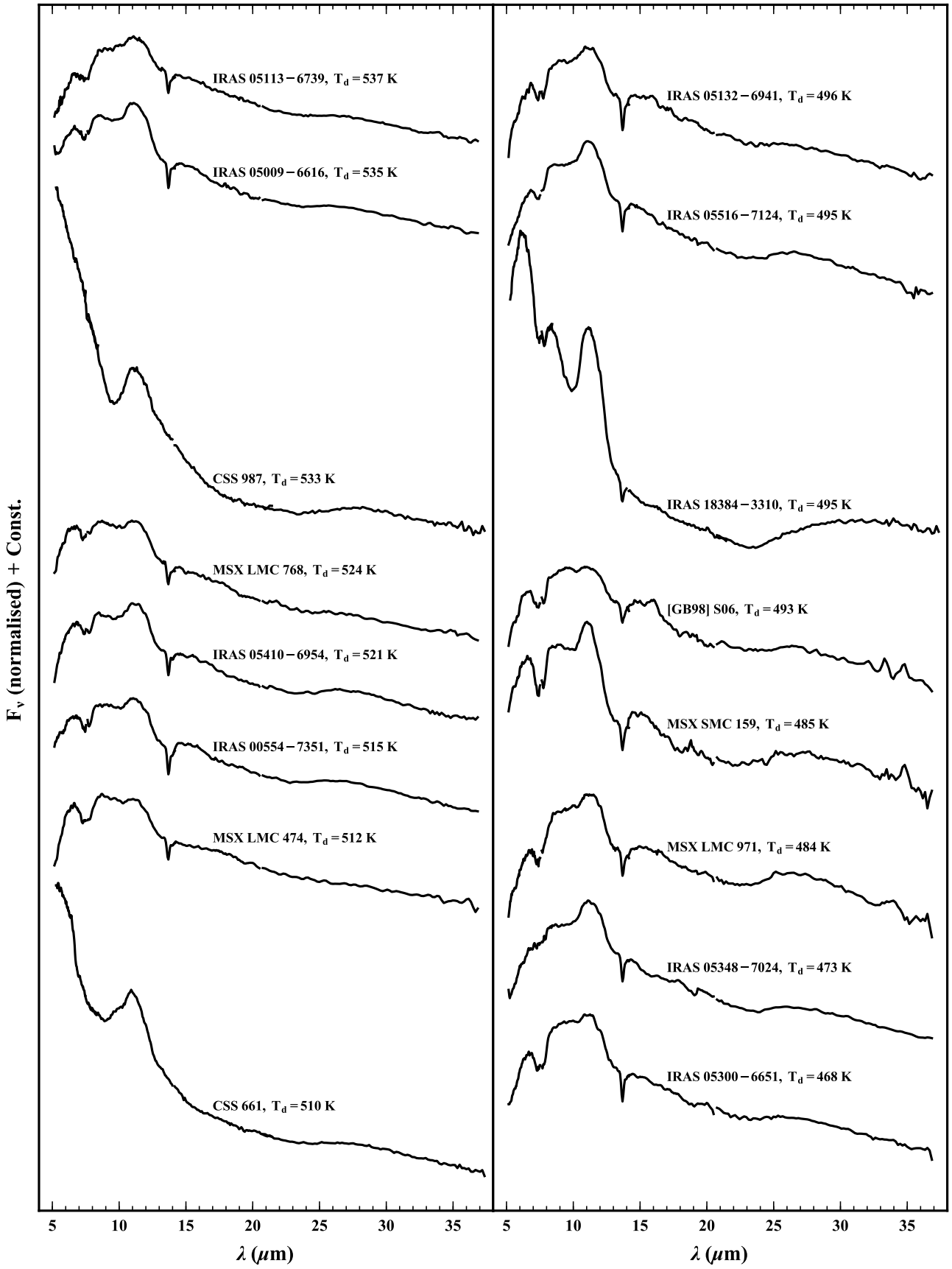

Fig. B.3. Overview of the *Spitzer* spectra (black solid lines) of the carbon-rich AGB stars with the 30 μm feature. The spectra are ordered according to the $T_{\rm d}$ from high to low temperature, top to bottom, and left to right, and are normalised to the flux density at 18 μm and offset for clarity. The names of objects and values of the $T_{\rm d}$ are shown above the spectra.

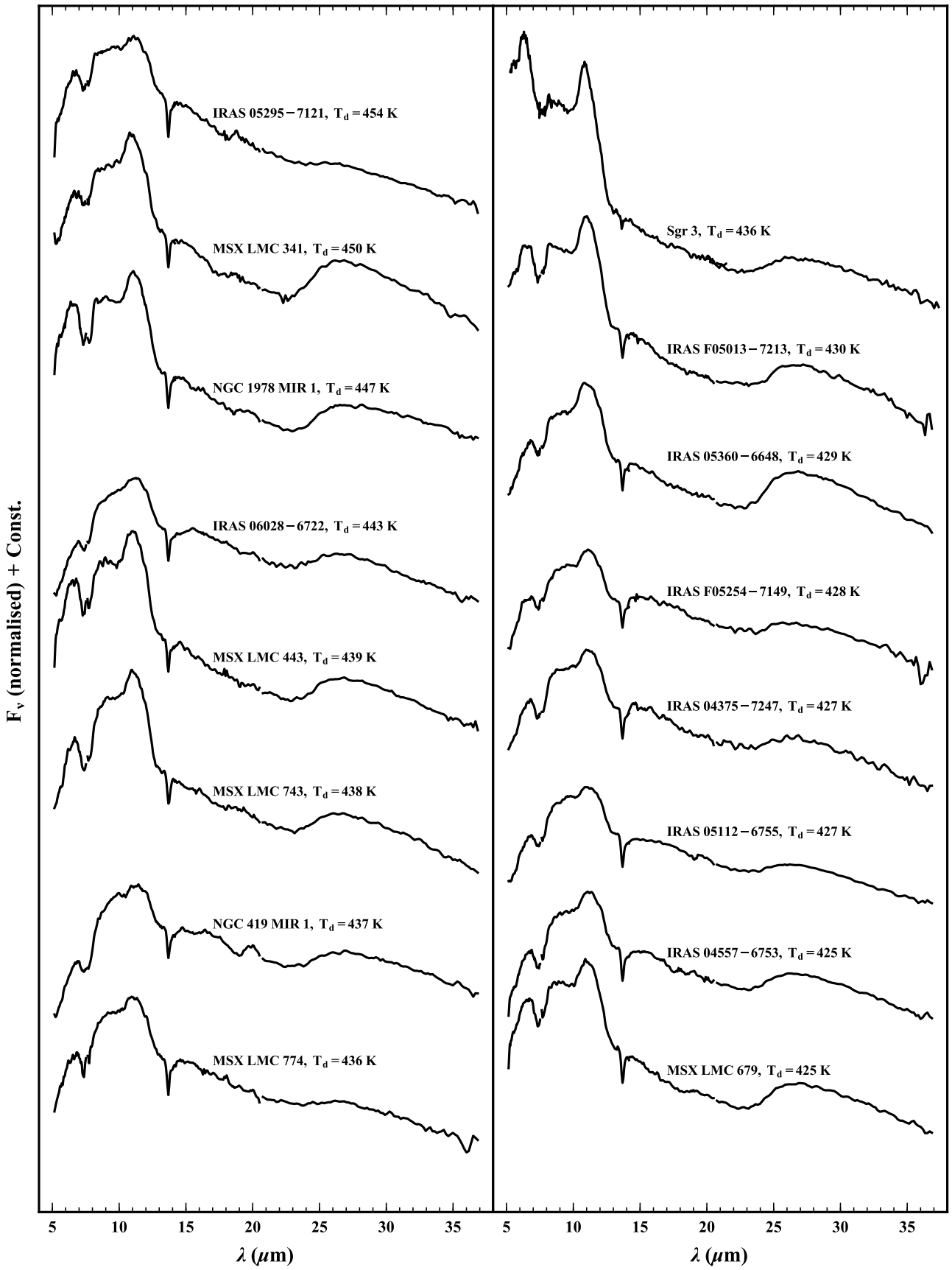

Fig. B.4. Overview of the *Spitzer* spectra (black solid lines) of the carbon-rich AGB stars with the 30 μm feature. The spectra are ordered according to the T_d from high to low temperature, top to bottom, and left to right, and are normalised to the flux density at 18 μm and offset for clarity. The names of objects and values of the T_d are shown above the spectra.

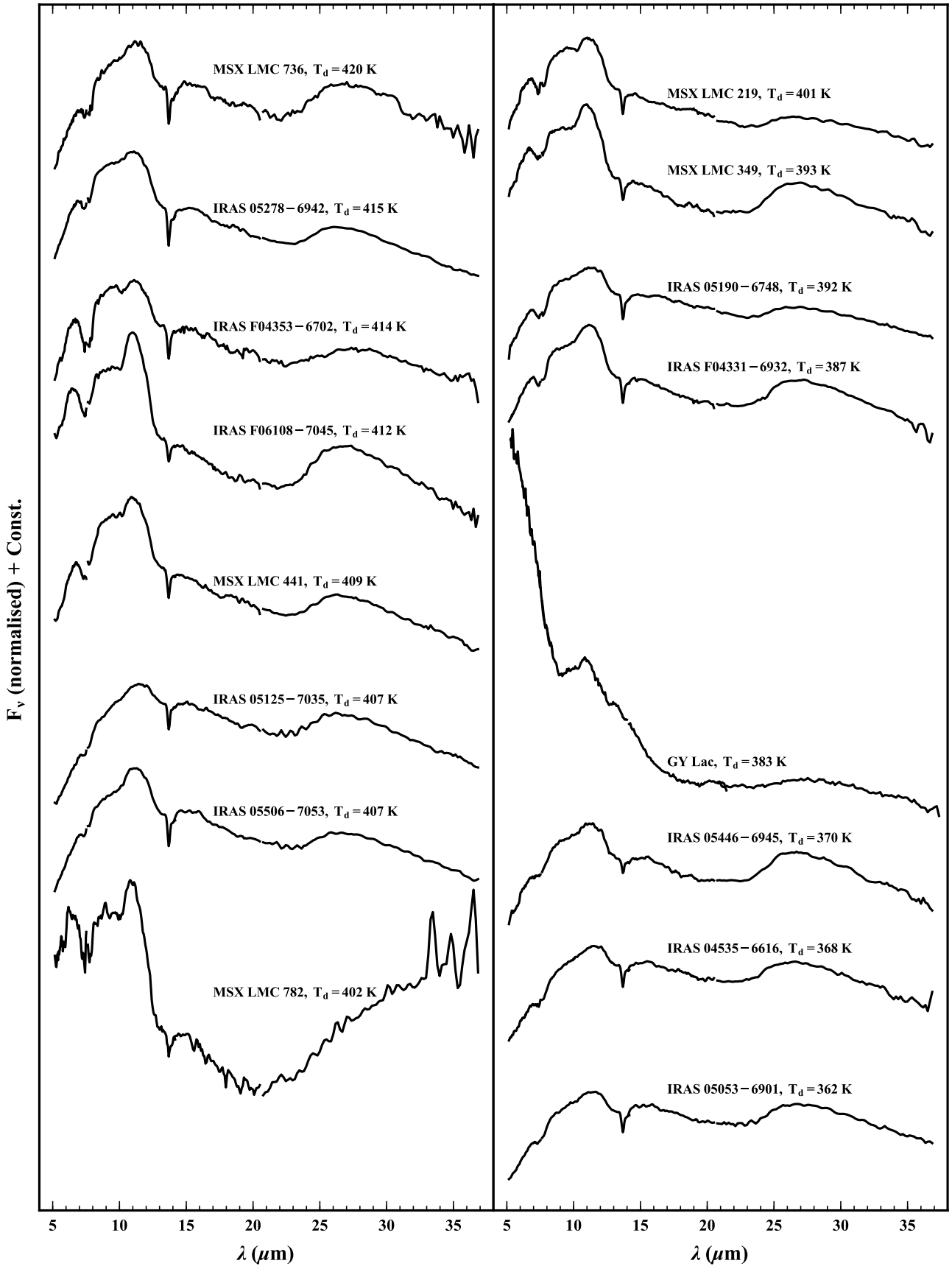

Fig. B.5. Overview of the *Spitzer* spectra (black solid lines) of the carbon-rich AGB stars with the 30 μm feature. The spectra are ordered according to the T_d from high to low temperature, top to bottom, and left to right, and are normalised to the flux density at 18 μm and offset for clarity. The names of objects and values of the T_d are shown above the spectra.

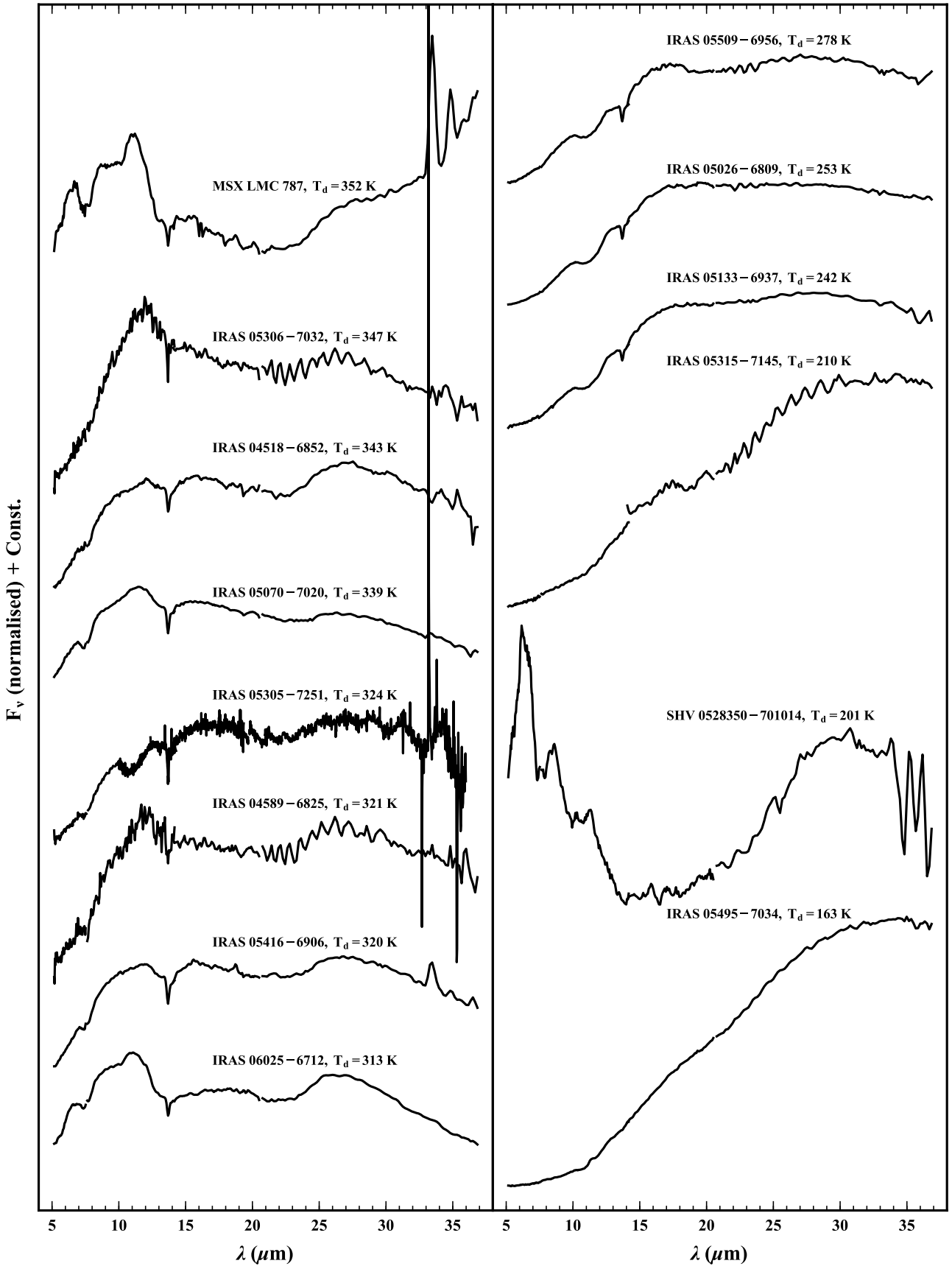

Fig. B.6. Overview of the *Spitzer* spectra (black solid lines) of the carbon-rich AGB stars with the 30 μm feature. The spectra are ordered according to the T_d from high to low temperature, top to bottom, and left to right, and are normalised to the flux density at 18 μm and offset for clarity. The names of objects and values of the T_d are shown above the spectra.

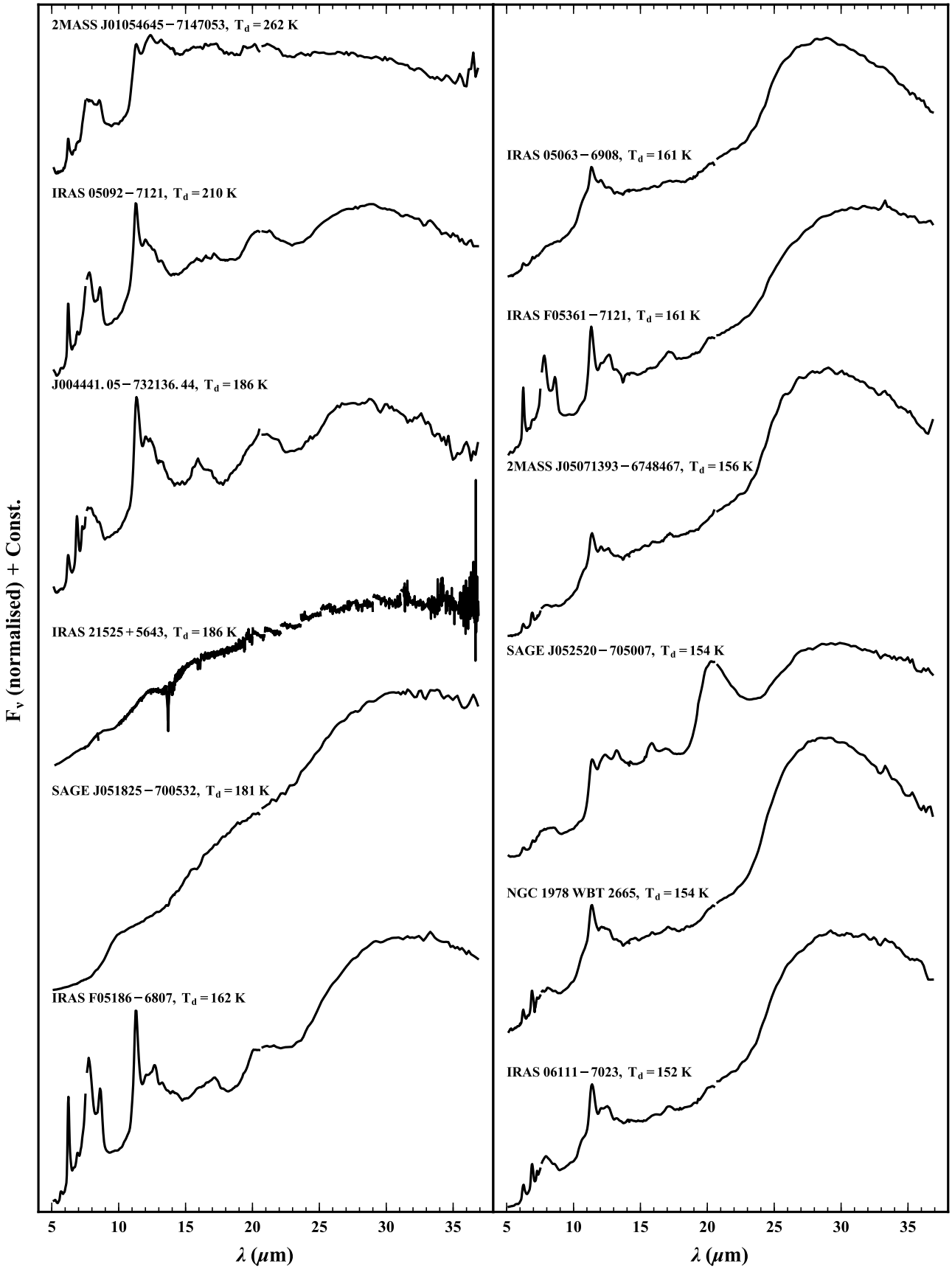

Fig. B.7. Overview of the *Spitzer* spectra (black solid lines) of the carbon-rich post-AGB stars with the 30 μm feature. The spectra are ordered according to the T_d from high to low temperature, top to bottom, and left to right, and are normalised to the flux density at 18 μm and offset for clarity. The names of objects and values of the T_d are shown above the spectra.

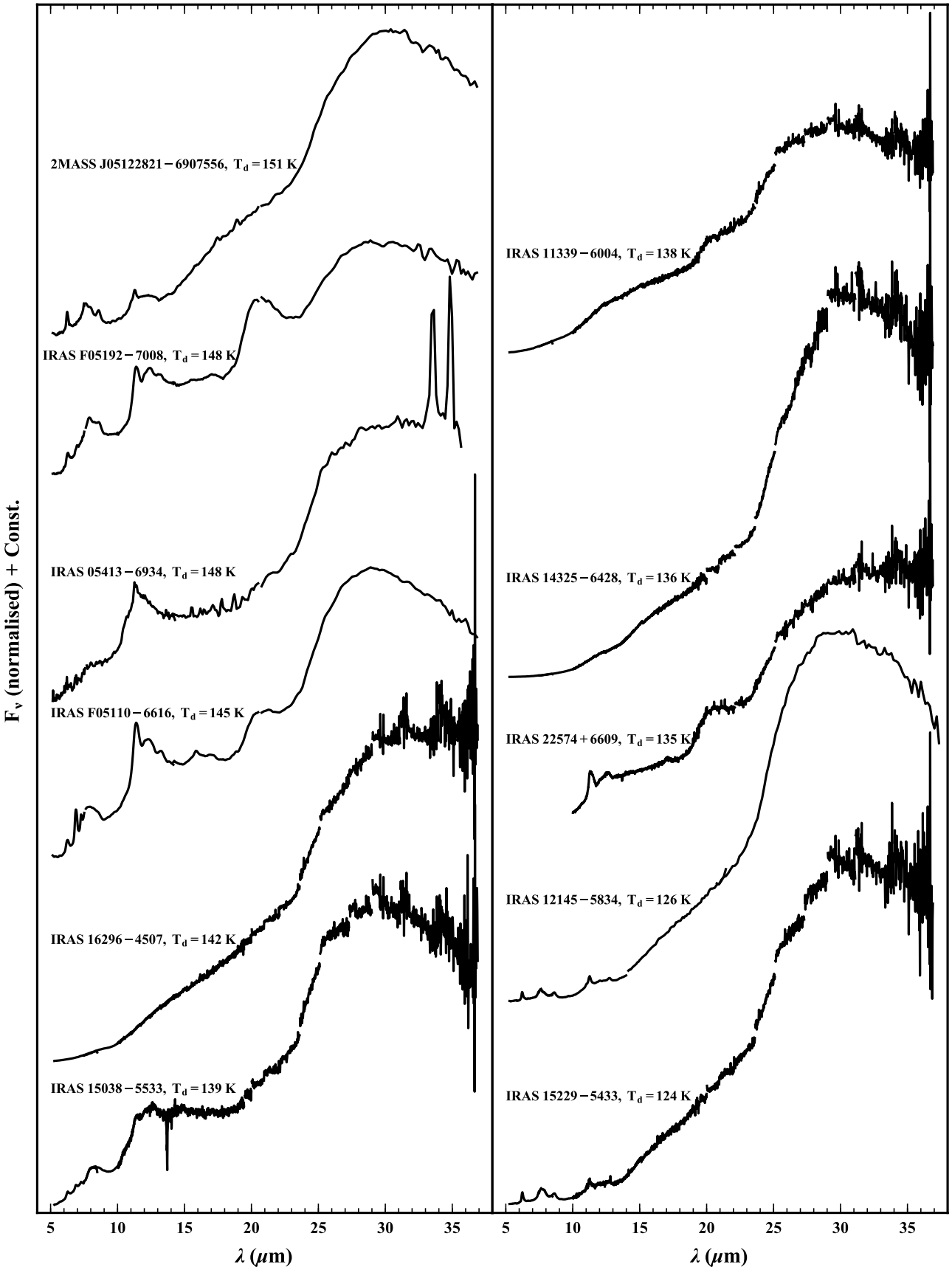

Fig. B.8. Overview of the *Spitzer* spectra (black solid lines) of the carbon-rich post-AGB stars with the 30 μm feature. The spectra are ordered according to the T_d from high to low temperature, top to bottom, and left to right, and are normalised to the flux density at 18 μm and offset for clarity. The names of objects and values of the T_d are shown above the spectra.

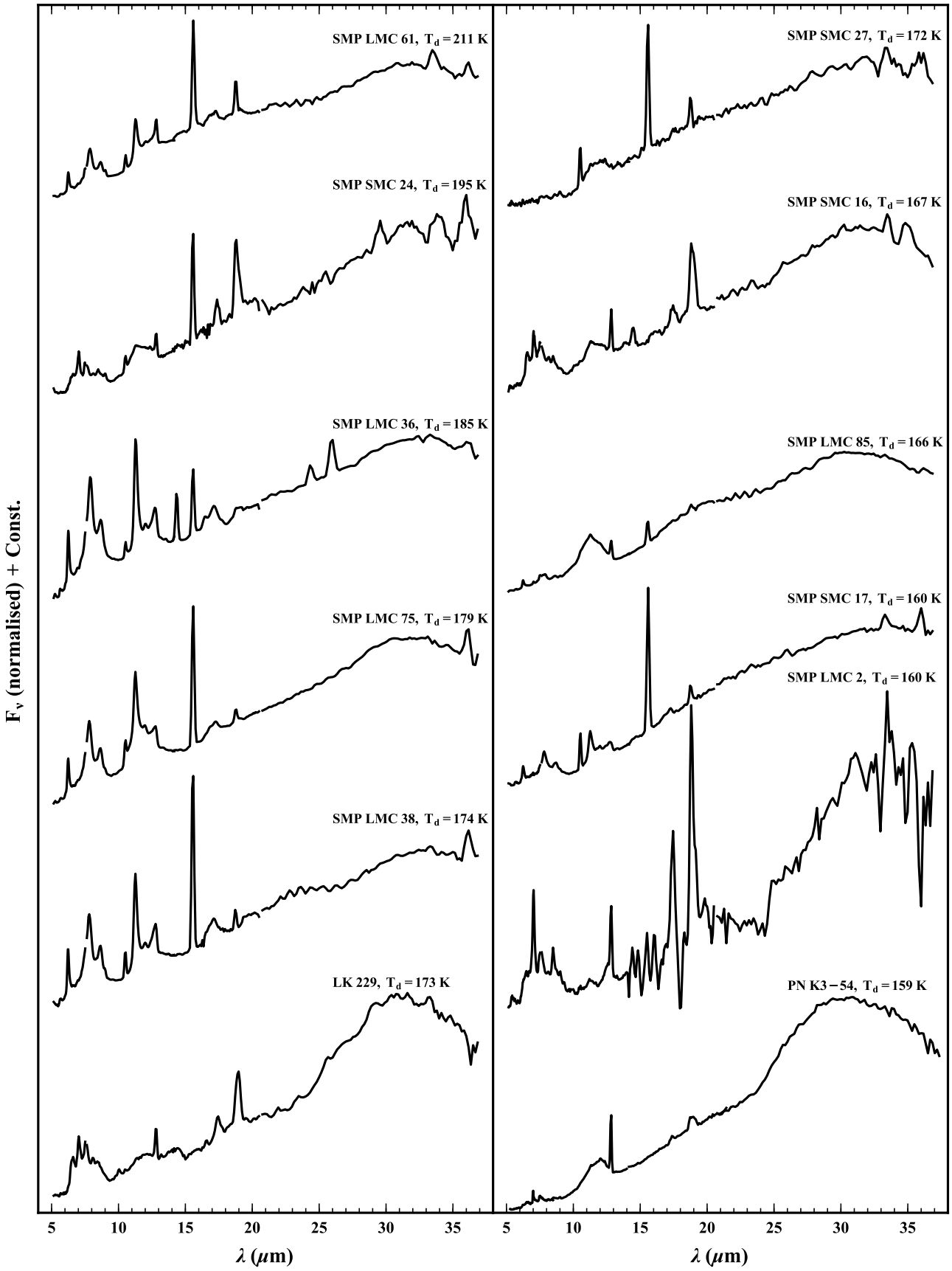

Fig. B.9. Overview of the *Spitzer* spectra (black solid lines) of the carbon-rich PNe with the 30 μm feature. The spectra are ordered according to the T_d from high to low temperature, top to bottom, and left to right. They are also normalised to the flux density at 18 μm (in case of SMP LMC 2 it is 18.4 μm) and offset for clarity. The names of objects and values of the T_d are shown above spectra.

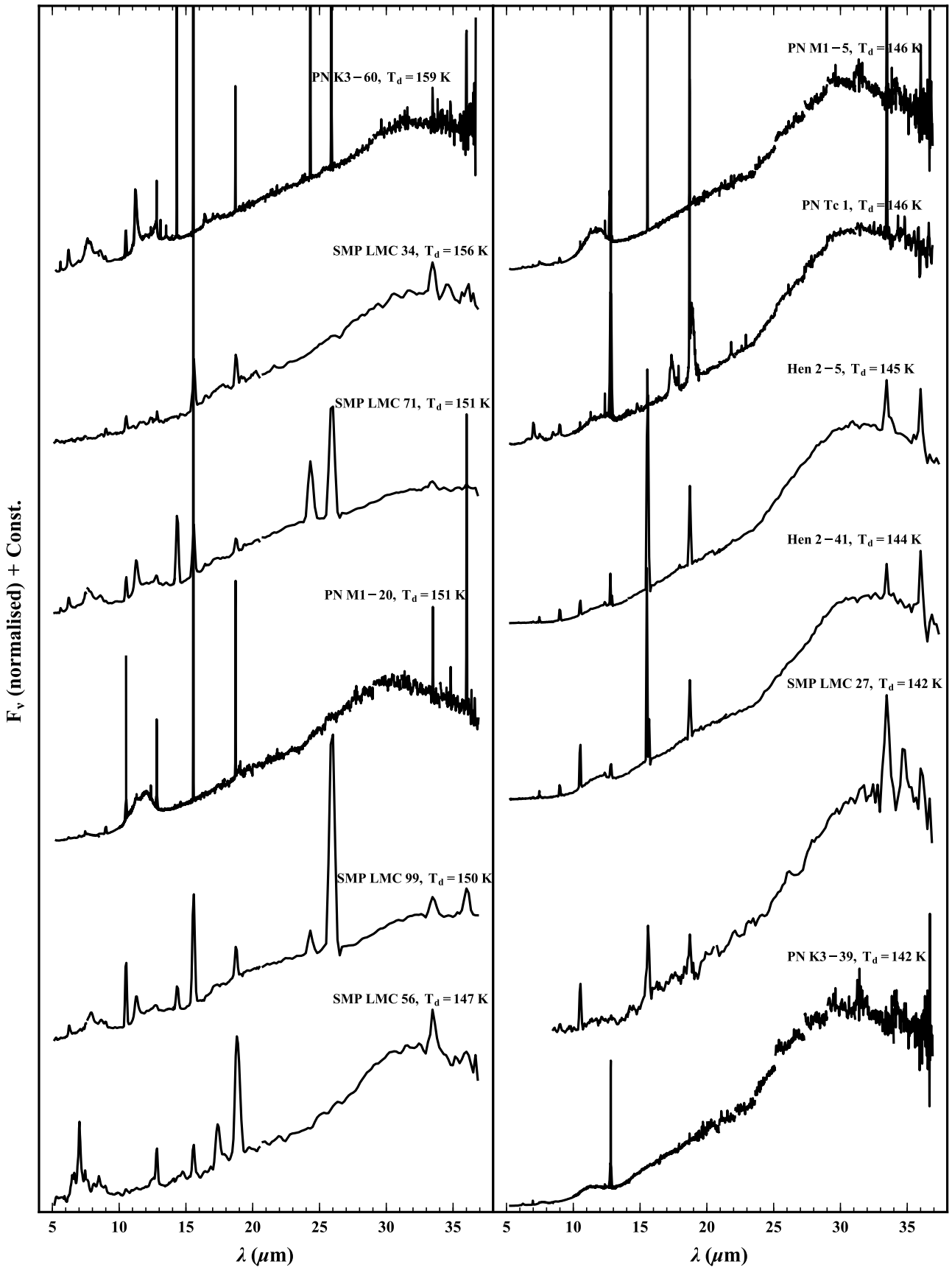

Fig. B.10. Overview of the *Spitzer* spectra (black solid lines) of the carbon-rich PNe with the 30 μm feature. The spectra are ordered according to the T_d from high to low temperature, top to bottom, and left to right, and are normalised to the flux density at 18 μm and offset for clarity. In case of SMP LMC 27, the part of spectrum between around 5–8.5 μm is not shown because it is very noisy and makes other spectra less readable in this region. The names of objects and values of the T_d are shown above the spectra.

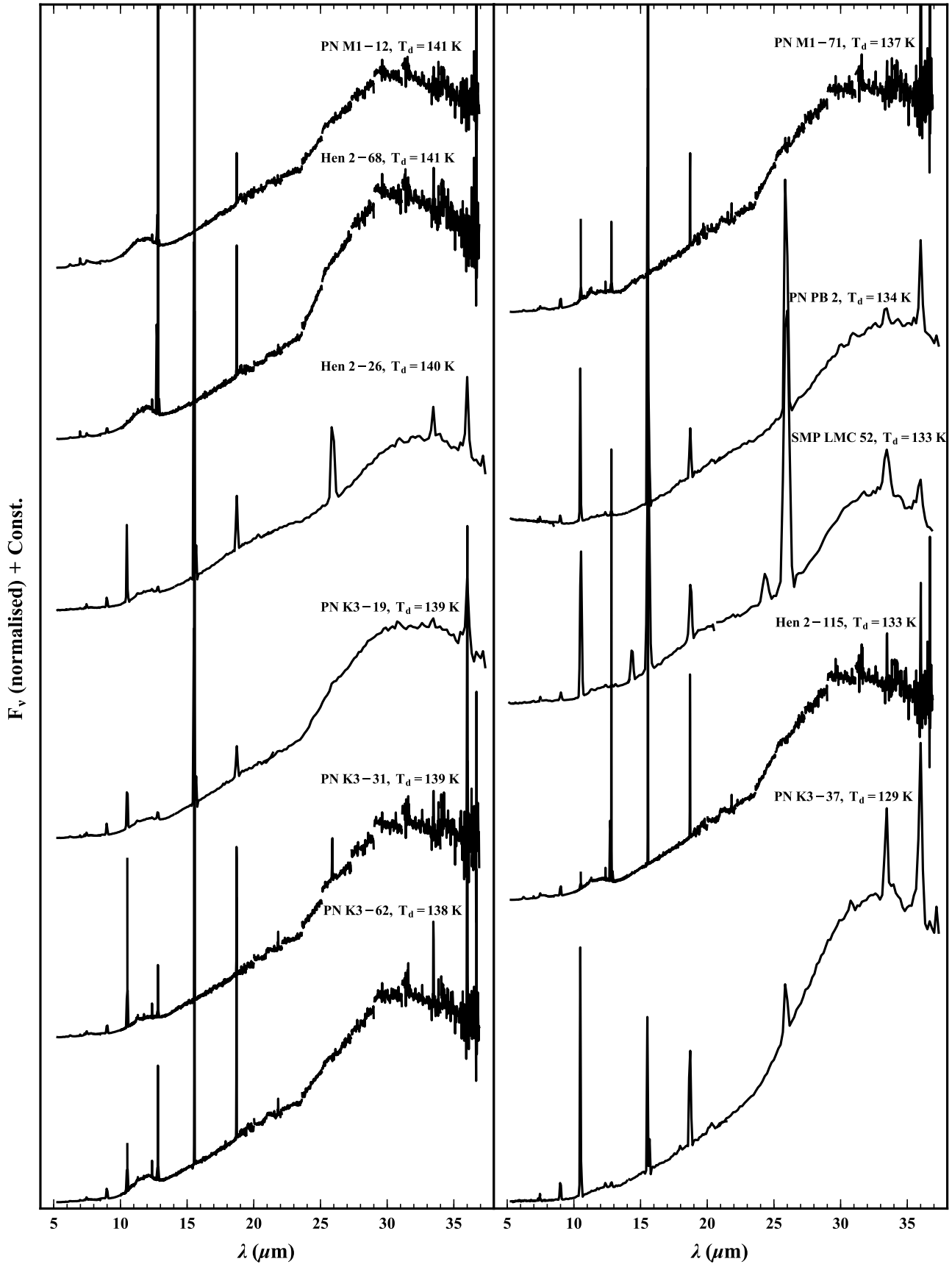

Fig. B.11. Overview of the *Spitzer* spectra (black solid lines) of the carbon-rich PNe with the 30 μm feature. The spectra are ordered according to the T_d from high to low temperature, top to bottom, and left to right, and are normalised to the flux density at 18 μm and offset for clarity. The names of objects and values of the T_d are shown above the spectra.

Appendix C: Normalised median profiles

In Sect. 4.2 we compare the normalised median profiles of the 30 μm feature for the AGB stars, post-AGB objects, and PNe (see Figs. 17–19). In Figs. C.1–C.15 we present the individual normalised profiles of the 30 μm feature, which are a part of every median profile shown in Figs. 17–19 (Sect. 4.2). The profiles for the AGB stars are illustrated in Figs C.1–C.9, whereas for post-AGB objects and PNe are shown in Figs. C.10–C.15, respectively. Furthermore, Figs. C.11–C.15 present the profiles of the 30 μm feature for the Galactic post-AGB objects and PNe derived from the high resolution *Spitzer* spectra. In each of figures presented here, we show the individual normalised profiles of the 30 μm feature by the solid grey lines, whereas the result median of all normalised profiles is presented on top by the coloured solid line with a colour consistent to the analysed galaxy (lime – SMC, red – LMC, gold – Sgr dSph, black – Milky Way).

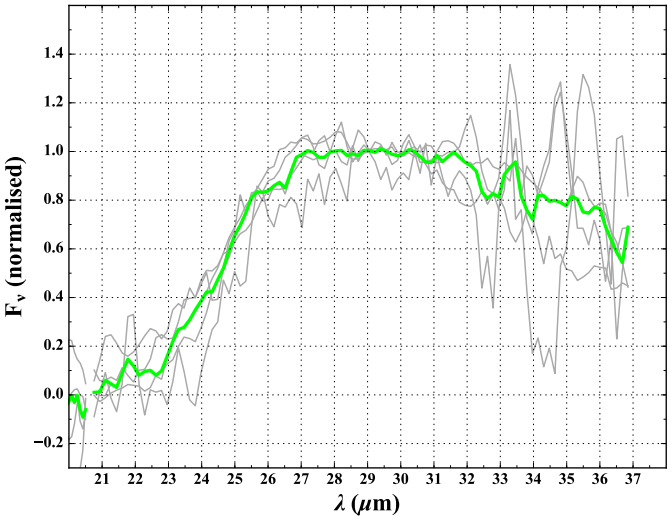

Fig. C.1. Normalised profiles of the 30 μm feature (grey solid lines) for the AGB stars in the SMC for which the obtained T_d is between 400 and 600 K. The normalised median profile of the feature is shown by the solid lime line.

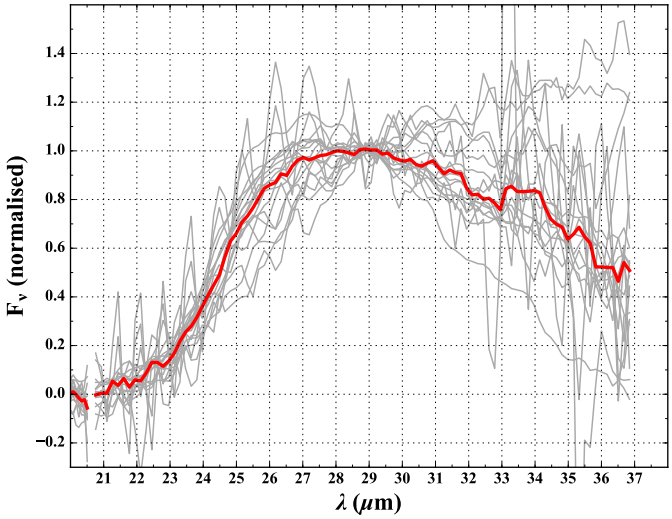

Fig. C.2. Normalised profiles of the 30 μm feature (grey solid lines) for the AGB stars in the LMC for which the obtained T_d is between 200 and 400 K. The normalised median profile of the feature is shown by the solid red line.

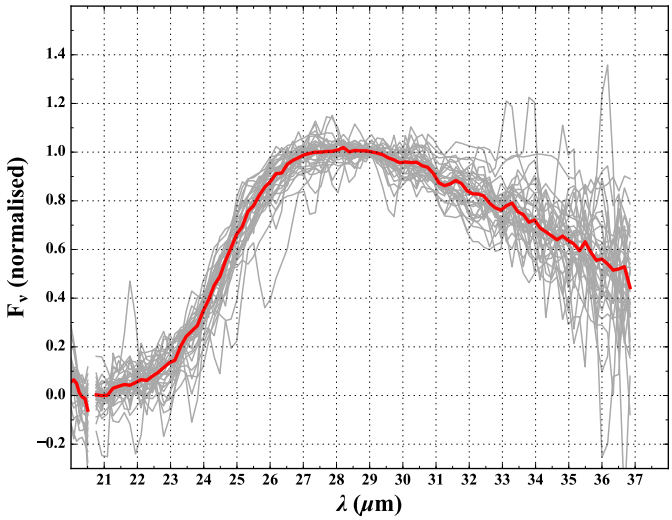

Fig. C.3. Normalised profiles of the 30 μm feature (grey solid lines) for the AGB stars in the LMC for which the obtained T_d is between 400 and 600 K. The normalised median profile of the feature is shown by the solid red line.

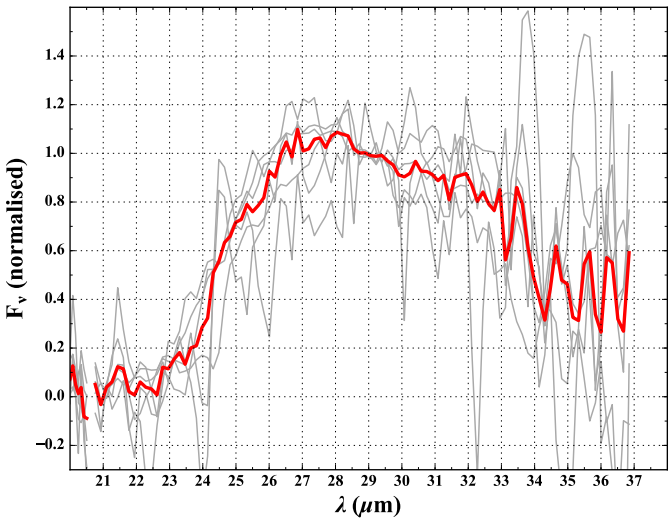

Fig. C.4. Normalised profiles of the 30 μm feature (grey solid lines) for the AGB stars in the LMC for which the obtained T_d is between 600 and 800 K. The normalised median profile of the feature is shown by the solid red line.

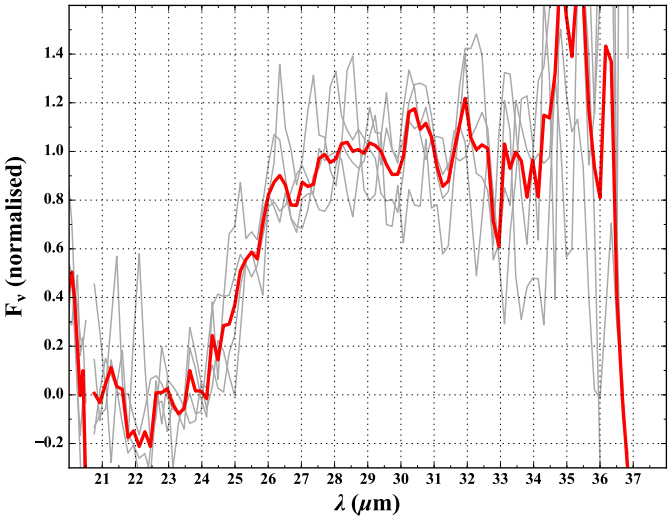

Fig. C.5. Normalised profiles of the 30 μm feature (grey solid lines) for the AGB stars in the LMC for which the obtained T_d is higher than 800 K. The normalised median profile of the feature is shown by the solid red line.

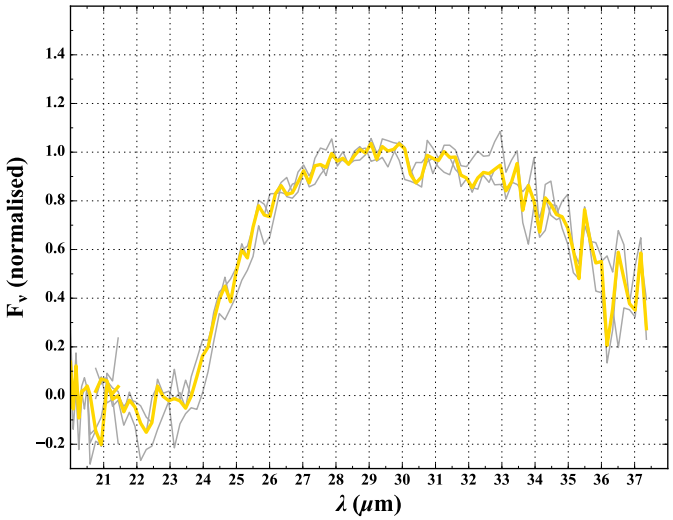

Fig. C.6. Normalised profiles of the 30 μm feature (grey solid lines) for the AGB stars in the Sgr dSph galaxy for which the obtained T_d is between 600 and 800 K. The normalised median profile of the feature is shown by the solid gold line.

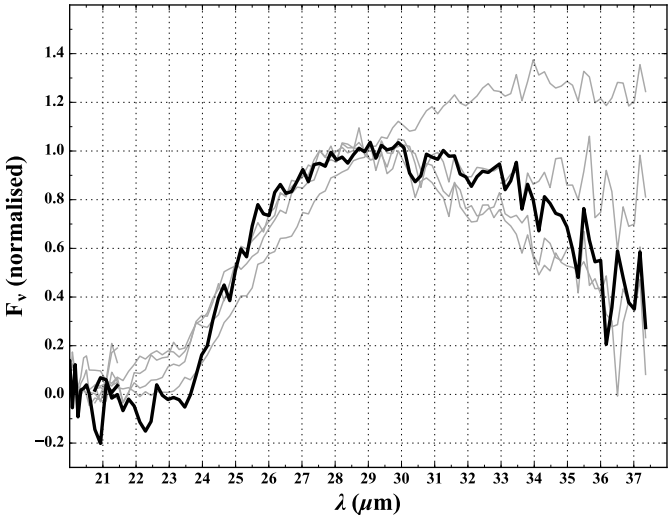

Fig. C.7. Normalised profiles of the 30 μm feature (grey solid lines) for the AGB stars in the Milky Way for which the obtained T_d is between 400 and 600 K. The normalised median profile of the feature is shown by the solid black line.

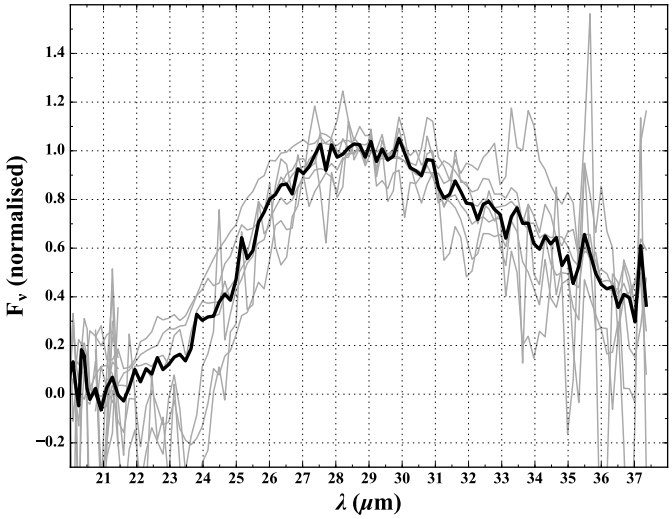

Fig. C.8. Normalised profiles of the 30 μm feature (grey solid lines) for the AGB stars in the Milky Way for which the obtained T_d is between 600 and 800 K. The normalised median profile of the feature is shown by the solid black line.

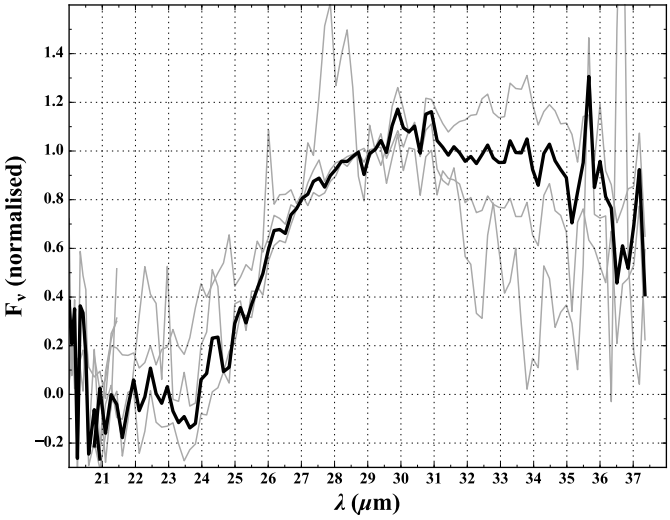

Fig. C.9. Normalised profiles of the 30 μm feature (grey solid lines) for the AGB stars in the Milky Way for which the obtained T_d is higher than 800 K. The normalised median profile of the feature is shown by the solid black line.

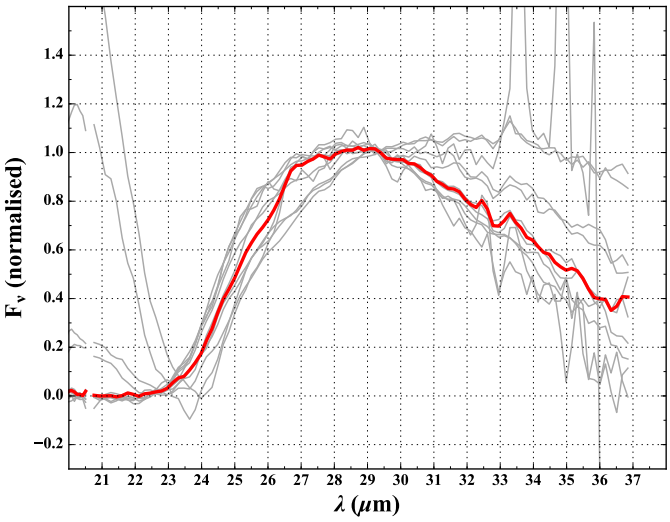

Fig. C.10. Normalised profiles of the 30 μm feature (grey solid lines) for the post-AGB stars in the LMC. The normalised median profile of the feature is shown by the solid red line.

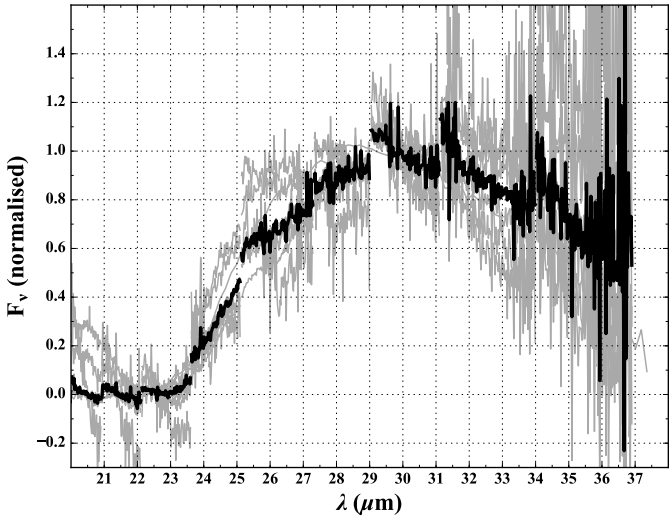

Fig. C.11. Low and high resolution normalised profiles of the 30 μm feature (grey solid lines) for the post-AGB stars in the Milky Way. The normalised median profile of the feature is shown by the solid black line. The low resolution normalised profiles are resampled to the high resolution wavelength grid using the linear interpolation.

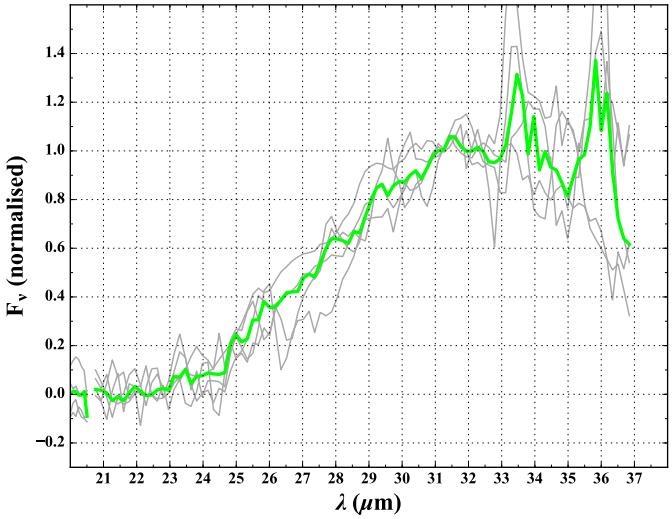

Fig. C.12. Normalised profiles of the 30 μm feature (grey solid lines) for the PNe in the SMC. The normalised median profile of the feature is shown by the solid lime line.

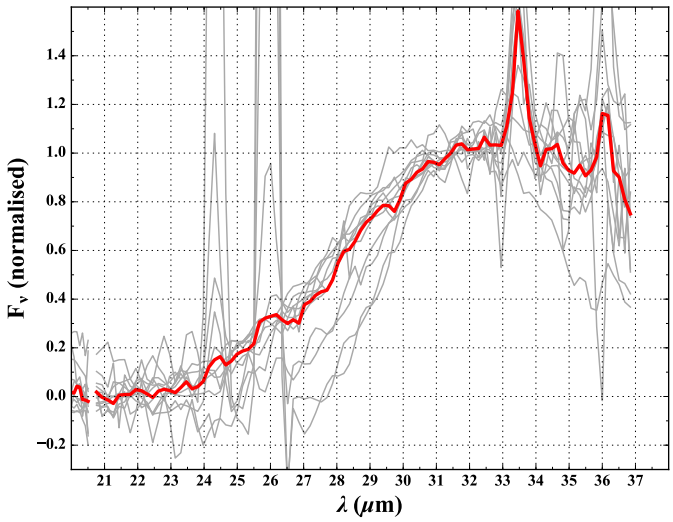

Fig. C.13. Normalised profiles of the 30 μm feature (grey solid lines) for the PNe in the LMC. The normalised median profile of the feature is shown by the solid red line.

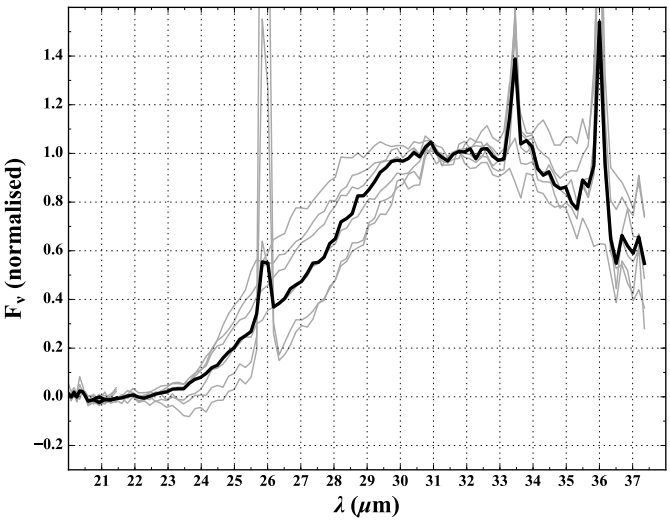

Fig. C.14. Low resolution normalised profiles of the 30 μm feature (grey solid lines) for the PNe in the Milky Way. The normalised median profile of the feature is shown by the solid black line.

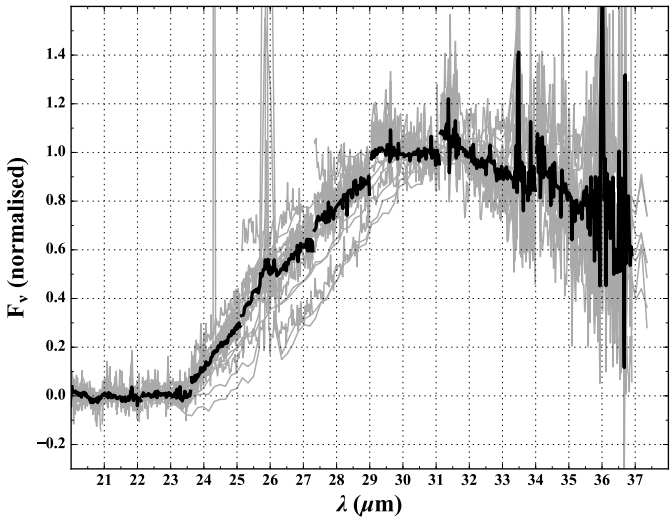

Fig. C.15. Low and high resolution normalised profiles of the 30 μm feature (grey solid lines) for the PNe in the Milky Way. The normalised median profile of the feature is shown by the solid black line. The low resolution normalised profiles are resampled to the high resolution wavelength grid using the linear interpolation.

Appendix D: Tables

In Sect. 2.1 we present Table 1 with basic information about objects in the Sgr dSph. Here, we list Tables D.1–D.3 with basic information about objects in the remaining galaxies: the SMC, LMC, and Milky Way. A brief description is also given in Sect. 2.1.

In Sect. 3.2 we show Table 5 with the results of the spectroscopic analysis for the objects in the Sgr dSph. Here, we list Tables D.4–D.6 with the spectroscopic results for the objects in the SMC, LMC, and Milky Way. A brief description is also given in Sect. 3.2. Tables D.1–D.6 are only available at the CDS.